PNAS

Supporting Information for
52,000 years of woolly rhinoceros population dynamics reveal extinction mechanisms.

Damien A. Fordham[1,2,3*], Stuart C Brown[1,4], Elisabetta Canteri[1,4], Jeremy J. Austin[1], Mark Lomolino[5], Sean Haythorne[1,6], Edward Armstrong[7], Hervé Bocherens[8,9], Andrea Manica[10], Alba Rey-Iglesia[4], Carsten Rahbek[2,3,11,12], David Nogues-Bravo[2], Eline D. Lorenzen[4]

*Corresponding author. Damien Fordham.
Email**:** damien.fordham@adelaide.edu.au

This PDF file includes:

Supporting text
Figures S1 to S22
Tables S1
Legends for Movies S1 to S2
Legend for Datasets S1
Legend for Software S1

SI References

Other supporting materials for this manuscript include the following:

Movies S1 to S2
Datasets S1
Software S1: https://osf.io/6F5MD/

Supporting Information Text

Materials and Methods

Fossils

Fossil records were compiled for the woolly rhinoceros (*Coelodonta antiquitatis*) for the Late Pleistocene and Holocene in Eurasia. All records were obtained from the literature and publicly available databases (CARD (1), Stage3 (2)). For each record, we obtained information on the geolocation, age, material dated (e.g. bone, collagen), and method of radiocarbon (^{14}C) dating. Records were excluded from further analysis if geolocation data was not available, if fossils were indirectly dated, or if the quality of dates was poor.

The quality of each record was scored according to type of dated material, stratigraphic association, and dating method (3). All high-quality records (Barnosky score > 10) were retained and calibrated using OxCal (4) and the IntCal13 calibration curve (5). For some older fossils with no associated radiocarbon dating error, we used the mean error of all fossils in the nearest 10,000-year time bin. We did this to avoid truncation in estimates of the potential realised climatic niches of woolly rhinoceros (6), described below. Importantly, none of these records (with inferred dating error) were used for any direct inference regarding extinction time or extinction location. Following compilation and quality control there were a total of 288 ^{14}C dated fossil records for woolly rhinoceros (Fig. S14; Dataset S1).

Climate data

Paleoclimate data were accessed using a high resolution (0.5° x 0.5°) terrestrial climate dataset for the period 60,000 BP to present (1950 C.E.) (7). These data were generated by temporally linking 42 discrete snapshot simulations from the HadCM3B-M2.1 coupled general circulation model (8). The HadCM3B-M2.1 model has a nominal atmospheric resolution of 3.75° x 2.75° and is run as a series of snapshots at 1000-year intervals between 0 (1950 C.E.) and 22,000 BP and 2000-year intervals between 22,000 and 60,000 BP. The HadCM3B-M2.1 model has been shown to accurately represent different aspects of the climate system in land and sea surface temperatures, precipitation, and ocean circulation (8). The snapshot simulations were linked using splines based on monthly climatologies, and then imposing interannual and millennial scale variability (e.g. Dansgaard-Oeschger (9) and Heinrich (10) events). The data were then bilinearly downscaled to 0.5° x 0.5° and bias-corrected using a simple delta (change-factor) method (7). Validation of the downscaled, bias corrected climate data utilised here shows good agreement with ice-core reconstructions of regional temperatures, particularly for the Bølling-Allerød and Younger Dryas (7). The data also show good agreement against observed data for annual mean standard deviations (SD) for both temperature and precipitation, particularly over Eurasia, with the major patterns of climate well represented (7). Ice-sheet dynamics are simulated in HadCM3B-M2 using the ICE-5G model (11). While, choice of ice-sheet reconstruction can influence millennial scale climate variability (12), the ICE-5G model is commonly used to reconstruct climate change from the last interglacial (13) and to identify biological responses to this climatic change (14).

We extracted monthly data for precipitation, temperature, latent heat flux, and snow depth (as snow water equivalent; SWE) for our study region (Fig. 1). This data was then used to generate 30-year averages of five climate variables at 17-year time steps (generation length for woolly rhinoceros; see below): (i) Annual total precipitation; (ii) Boreal summer (JJA) average temperature; (iii) Boreal winter (DJF) average temperature; (iv) total evapotranspiration during Boreal spring and summer (MAM + JJA); and (v) Boreal winter average snow depth. These variables were chosen due to having likely ecological roles in the range dynamics of Eurasian megafauna (15, 16), including woolly rhinoceros. For example, woolly rhinoceros is thought to have preferred colder and drier areas with light snow cover and open steppe-tundra floral communities (17-19). Spatiotemporal information on evapotranspiration was considered because it is a proxy for plant growth (20).

Evapotranspiration was calculated by dividing the average monthly latent heat flux by the latent heat of vaporisation based on average monthly temperatures:

$$\text{ET (mm/month)} = \left(\frac{\text{heat flux}}{(2.501 - 0.00237 \times \text{tas}) \times 1e6}\right) \times 86400 \times 30 \qquad \text{Eq. 1}$$

Where *heat flux* and *tas* are the modelled monthly heat flux (W m^2) and temperature (°C) for each month from Armstrong, Hopcroft and Valdes (7).

Boreal winter average snow depth was converted from snow water equivalent to metres by multiplying the values by 4, assuming an average density of lying snow of 250 kg/m^3. Snow depth was then bias-corrected using monthly mean snow depth data (21). 100-year climatological monthly averages were calculated for the period 1850 – 1950 C.E. for both the Armstrong, Hopcroft and Valdes (7) and Compo*, et al.* (21) datasets, before a multiplicative change factor correction was applied. The bias correction scaling of snow depth was capped at three times the modelled value (7).

Information for both summer and winter temperatures was considered due to the broad geographical range of the species meaning that it was likely exposed to broad climatic conditions across its range, and that woolly rhinoceros was likely capable of some level of ecological plasticity (22). Furthermore, tolerance to winter temperatures is a major determinant of geographic range for northern hemisphere herbivores (23-25). Precipitation was considered because warmer, and wetter conditions are likely have negatively affected survival of woolly rhinoceros during the last deglaciation, resulting in a decline in suitable habitat, causing a downward pressure on abundance (26). Precipitation is also correlated with plant growth and thus food availability in temperate, boreal, and tundra ecosystems across Eurasia (27, 28). Boreal spring and summer evapotranspiration was considered because it is the time of year when plant growth is highest in forested, grassland, and tundra systems in Eurasia (29-31). Snow depth was considered because of the morphology of the woolly rhinoceros, where a large body and relatively short legs meant that it was not well adapted to deep snow cover (32, 33). While its front horn is likely to have been used to expose grazing vegetation covered in shallow loose snow, it is unlikely that it could have been used to access food under or to plough through deep or icy snow (34).

Dynamic Spatial Structure

Climate suitability was used to define the initial spatial structure for our process-explicit model. This was done by first reconstructing the ecological niche of woolly rhinoceros, using a 4-dimensional hypervolume (35) and multi-temporal approach (36). Our multi-temporal approach captured occurrence climate relationships over a long period of time (> 50,000 years), including periods when modern humans were low in abundance in Eurasia (37). This limited environmental suitability from being truncated owing to human-driven local extinctions in otherwise suitable areas (6). Directly accounting for uncertainties in fossil ages in the climate co-occurrence data resulted in a wide representation of climate conditions in the 4-dimensional hypervolume (38-40), providing a purposely broad prediction of the potential climatic niche of the woolly rhinoceros — the climatic space where the species could have lived (36).

Woolly rhinoceros niche

We 'merged' fossil records where there was spatiotemporal overlap within each 1° x 1° grid-cell. To do this, longitude and latitude values for fossils (Data S1) were rounded to one decimal place (retaining ~11.1 km of accuracy) and grouped. Each record was then checked for temporal overlap with all other records in the same group. Temporal overlap was defined as overlapping confidence intervals for the calibrated radiocarbon ages (Calibrated Age ± 1 S.D.). Where temporal overlap occurred, the confidence intervals were merged for all overlapping records resulting in a single record with an expanded age interval (38). For example:

> at site X there are 3 records with calibrated ages of: record 1 = 19,213 – 16,933; record 2 = 19,638 – 18,366; and record 3 = 14,706 – 13,888 B.P. There is overlap in the confidence intervals for records 1 and 2. Removing the temporal overlap thus results in only 2 records at site X – the 2 remaining records would have calibrated ages of: record [1 & 2] = 19,638 – 16,933 and record 3 = 14,706 – 13,888 BP.

Pre-processing the collated fossil records using this approach reduced the number of records for modelling the climatic niche from 288 to 244 for woolly rhinoceros (Fig. S15).

We intersected each georeferenced fossil with climate data (for the five variables described above) for the period ± 1 SD around the estimated calibrated ^{14}C age of the fossil (39). This was done to ensure that each fossil had a time series of climate data associated with it for the window of uncertainty surrounding its calibrated ^{14}C date. Climate variables were calculated as the average values from the cell containing the fossil and the 8-surrounding cells. The 9-cell averaging approach was chosen to minimise fine scale artificial accuracy/biases introduced during the bias correction and downscaling of the climate data (7). The resulting climatic information represents the climate history over which woolly rhinoceros was likely to have been present at the fossil sites (38, 39).

Woolly rhinoceros was not adapted to surviving in areas of deep snow (32, 33), particularly as extreme winter conditions limit access to food, reduce fecundity, and increase mortality (24, 25). Exploratory analysis between fossil locations and areas of deep snow (>1.5 m) suggested that the inclusion of snow as an additional fifth hypervolume parameter would show little improvement in the modelled niche of the species. Therefore, we opted to rather use snow depth as a friction layer for dispersal within our simulations (17, 41).

This fossil-climate data was used to generate a multi-temporal approximation of the full potential niche of the woolly rhino using the hypervolume package for R (42) and the “gaussian” hypervolume method (43), with bandwidths, number of standard deviations, and the probability threshold tuned through cross-validation. Gaussian hypervolumes were built by defining a Gaussian kernel density estimate on an adaptive grid of random n-dimensional points around the original data points. The bandwidth, number of standard deviations, and the probability threshold controlled the size and configuration of the kernel density estimate (42, 43). The resulting hypervolume of climate suitability was exhaustively subsampled, allowing the realised niche of the woolly rhino to be identified using process-explicit macroecological modelling (see below).

To do this we exhaustively subsampled the full multi-temporal niche hypervolume by subsampling ‘boxes’ with different widths (from 0.5 to 0.95, every 0.05), moving throughout the 4-dimensional space. To obtain unique niche subsamples, the climate variables were rounded to 1 decimal place and subsampled niches that were identical in all 4 dimensions were removed. This process generated 54,124 unique niche subsamples, each representing a conceivable realised niche for the woolly rhinoceros. All niche subsamples were constrained to the 4-dimensional space of the full (multi-temporal) potential climatic niche.

Based on (44) we calculated the marginality of each unique niche subsample using the ade4 R package (45). Here, marginality is a measure of climatic specialisation, calculated using the distance between the climate conditions of the niche subsample and the mean conditions of the full potential climatic niche (38). High marginality values correspond to niche subsamples that have less common climatic conditions compared to the full potential climatic niche and its background, while low values represent non-marginal niches with climates that are typical of the full potential climatic niche and its background. Niche volume was calculated as the volume of the gaussian hypervolumes (43). Measures of marginality and niche volume were then used to further subset the 54,124 niche subsamples, ensuring even representation of both metrics. To do this we transformed both measures of niche marginality and volume from their original values to a uniform distribution by (i) ranking the raw values, (ii) converting to a probability, and then (iii) mapped the probabilities to a uniform distribution $\left(\rho = \mathrm{U}(0, 1)\right)$. We subsampled (without replacement) 2,999 niche cuts, ensuring that both the original and uniform distribution of values was maintained (Fig. S16). The full potential climatic niche was included, giving 3,000 potentially plausible realized ecological niche models for woolly rhinoceros.

Climate suitability projections

Spatiotemporally explicit projections of probability density (hereafter, habitat suitability) were then created at generational time steps using each plausible ecological niche model (n = 3,000) from 60 ka BP to 8.0 ka BP for woolly rhinoceros. The approach assumes that the distribution of a given species is a spatial indicator of its ecological requirements (46). Projections were created using the hypervolume package (43). Comparisons between spatial projections of habitat

suitability from the hypervolume package, and more common maximum entropy methods (47) have shown comparable results (43).

Cross-validation was used to validate the full multi-temporal ecological niche model and to tune the two parameters that effect habitat suitability: (i) weight.exponent, and (ii) edges.zero.distance.factor. These two parameters control the rate and distance at which habitat suitability reduces to 0 from its empirical maximum. Cross-validation folds were defined as10 unique subsets of the fossil record across space and time. For each cross-validation fold we did a grid search over both parameters (edges.zero.distance.factor range = 1:10; weight.exponent range = -1:-3), extracted values of habitat suitability at fossil locations (temporally explicit), and then calculated the Boyce Index (48, 49). The Boyce index is a presence-only evaluation measure used to discriminate how much projections of habitat suitability at presence locations differ from random expectation. Higher Boyce values indicate greater habitat suitability at presence locations than expected by chance. Final parameters were chosen based on the combination of parameters that maximised the Boyce Index (mean Boyce Index = 0.87 (±0.13)) and consequently habitat suitability at fossil locations through time. Following cross-validation the weight.exponent was set to -3 and edges.zero.distance.factor was set to 5. These settings were then used for each of the 3,000 ecological niche models.

Since the outputs of the *hypervolume_project* function are not bound by [0, 1] (42, 43), each of the projections of habitat suitability was then rescaled to the range 0-1 using the formula:

$$x_r = \frac{x\text{-}\min(x)}{P_{95\%}(x > 0) - \min(x)} \qquad \text{Eq. 2}$$

Where x_r is the rescaled suitability value, x is the original value, min(x) is the smallest value for x, and $P_{95\%}$ is the 95th percentile of all x values > 0. We opted to rescale based on the 95th percentile of suitability values (exc. 0) due to the number of cells with habitat suitability values of zero, and the extreme right skew of the suitability values inflating the maximum value. Projections of habitat suitability were then reprojected using bilinear interpolation to a Lambert Azimuthal Equal Area projection centred on 104° east and 60° north, with a resolution of 100 km x 100 km.

To ensure that models of climate suitability captured the tolerance of woolly rhinoceros to warm temperatures, we generated projections at the Eemian (last interglacial) – a period when temperatures at high latitudes were as warm or warmer then today (50). Projections (based on the full potential climatic niche) showed that our multi-temporal niche modelling approach sufficiently captured upper temperature tolerance in its projections of climatic suitability, with vast areas of the landscape having suitable habitat for the woolly rhinoceros at 120 ka BP (Fig. S11). Further tests, using process-explicit models also confirmed that our quantification of climatic tolerance for woolly rhinoceros enables survival during past warm events that it persisted through (see below).

Human density

We modelled the peopling of Eurasia using the Climate Informed Spatial Genetic Model (CISGeM), where human density (modelled as local effective population size; N_e) is forced by paleoclimatic reconstructions of net primary productivity (NPP), genetic history, and local demography (51, 52). CISGeM has accurately reconstructed the arrival times of anatomically modern humans and contemporary distributions of global and regional genetic diversity (51, 52). Furthermore, it has been coupled to macroecological models to explore megafauna-human interactions (38-40).

CISGeM models the globe on a 100 km (10,000 km^2) equal area hexagonal grid. The carrying capacity of each grid cell is determined by reconstructions of paleo temperature and precipitation which are used to predict NPP values using the Miami NPP model (53). The Miami NPP model provides a good first order characterisation of ecosystem productivity, despite not accounting for seasonality or the explicit effects of CO_2, humidity, or plant and soil types. NPP from the Miami model is defined as the minimum of temperature and precipitation limited rates of annual NPP:

$$NPP = \min(NPP_t, NPP_p)$$
with,
$$NPP_t = 3000 \times (1 + \exp(1.315 - 0.119 \times tas))^{-1}$$
$$NPP_p = 3000 \times (1 - \exp(-0.000664 \times prec))$$

Eq. 3

Where, *tas* is equal to the annual average air temperature (°C), and *prec* is the total annual precipitation (mm) for a given grid cell.

For the period 120 ka BP to 60 ka BP, we utilised the previous global NPP reconstructions generated with the HadCM3 model (51), from 60 ka BP to 0 BP we blended the previous reconstructions with NPP calculated using the paleoclimate reconstructions from Armstrong, Hopcroft and Valdes (7) for the northern hemisphere. As the Armstrong, Hopcroft and Valdes (7) data starts at 60 ka BP, to generate a seamless transition between the simulated NPP values at this time we calculated anomalies on annual average NPP over a 100-generation (2,500 year) period of overlap (60 – 57.5 ka BP) between the previous reconstructions and our modelled NPP. The anomalies were then applied to the Armstrong, Hopcroft and Valdes (7) data to keep values consistent with those estimated from the HadCM3 model which had been used previously (Fig. S17). A similar approach has been used elsewhere (54).

CISGeM allows inhabited cells to grow at rate *r* until the local carrying capacity is reached. Once carrying capacity is reached, migrants are sent to other inhabited cells at rate *m*, or allowed to colonise nearby previously uninhabited cells at rate *c*. The relationship between carrying capacity and the demographic parameters underlying CISGeM have previously been determined (51) using Approximate Bayesian Computation (55) in a pattern-oriented framework (56).

Using the ABC fit from Eriksson*, et al.* (51), we took the best 4,900 parameter combinations and reconstructed human N_e through time for modelling the human impact on woolly rhinoceros (39). For each grid-cell in our study region we used CISGeM to calculate a time-series of population size from 120 – 0 ka BP at 25-year time steps. To account for parameter uncertainty in spatiotemporal projections of N_e we ran 4,900 different models using the previously established parameters (51). We calculated the mean and standard deviation for population size in each grid cell at each time point from 60 ka BP. The mean and standard deviation of N_e were then reprojected to the same 100km × 100km equal area projection as our reconstructions of habitat suitability. N_e values were scaled between 0 and 1 (using the 95th percentile of maximum values as the upper bound; 38). The CISGeM outputs at their original 25-year timesteps were then linearly interpolated to annual timesteps, so that we could generate 30-yr averages at 17-year steps to match the temporal resolution of the habitat suitability projections. We then generated 45,000 plausible reconstructions of human population abundance, by sampling within ± 1 SD of N_e using a log-normal distribution. Stochasticity in human abundances in our simulations is therefore the result of sampling established ranges for demographic parameters in CISGeM.

Woolly rhino-climate-human interactions

Ecological niche models of habitat suitability and CISGeM estimates of human abundance were coupled with stochastic demographic models to simulate climate-human- woolly rhino interactions. Driver-state relationships simulated the effects of climate change and hunting by humans on key ecological processes of extinction: niche lability, dispersal, population growth and Allee effect. The spatially explicit population models (SEPMs) were built using the R packages poems (57) and paleopop (58), using a framework developed to identify drivers and ecological processes of megafauna extinctions (39). Here scalar-type SEPMs centred on 'best estimates' for demographic processes (population growth rate and its variance, dispersal, Allee effect), environmental attributes (niche breadth and climatic specialisation) and threats (human abundance and rates of exploitation) are simulated across wide but plausible ranges. Pattern-oriented modelling (56) is used to evaluate different model versions and parameterisation, by cross-matching simulations with inferences from paleo-archives (39). Code to run an example population model is available here: https://osf.io/6F5MD/.

Population model

Below we describe estimates of demographic parameters and their ranges (Table S1) used in the woolly rhinoceros SEPM.

Generation lengths

The SEPM simulates climate-human-woolly rhino interactions at 17-year generational time steps. Our estimate of a generation length of 17 years for the woolly rhinoceros is based on generation lengths for the most closely related extant species (Sumatran rhinoceros; *Dicerorhinus sumatrensis*) (59), and the closest extant species with a comparable body size (white rhinoceros; *Ceratotherium simum*). The generation length for the two related species is estimated to be 15–20 years for Sumatran rhinoceros and 15–19 years for the White Rhinoceros (60, 61), depending on how generation length is calculated.

Upper abundances

The upper abundance (i.e. carrying capacity) of each grid-cell in our models was based on habitat suitability (62). We converted habitat suitability to carrying capacity by assuming that the maximum area of suitable habitat in any given grid-cell was 2,500 km^2 and not 10,000 km^2. This approach was necessary to address the mismatch between the spatial scale of the model (100 km × 100 km) and how megafauna are likely to have used the landscape (39). We allowed maximum upper abundance to vary between 75 and 32,500 rhinos (corresponding to .03 rhinos/km^2 and 13 rhinos/km^2, assuming that only 25% of a cell is useable). These values, for extant species (Sumatran rhinoceros, white rhinoceros), come from monitored populations in areas of high habitat suitability (63-67).

Population growth and variance

Generational population growth rate in the scalar SEPM was estimated using a vortex model for Sumatran rhinoceros (66), where maximum annual growth rate was estimated to vary between 0.008 to 0.031. We calculated generational R_{max} using $exp(r)^{17}$ (where 17 is equal to the generation length of the species) and treated this as an upper estimate of R_{max} in the model. Generational R_{max} based on the Sumatran rhinoceros therefore ranged from 1.146 – 1.694. We also used allometry to estimate R_{max}. The upper and lower bounds were subsequently set at 1.00 – 2.00.

To estimate variability in population growth we built an aspatial annual-scalar population model with a Ricker logistic population function (68). The Ricker-logistic function was chosen because it assumes an almost exponential growth rate when population abundances are small and predicts a decrease in population growth rate when populations approach carrying capacity, reflecting competition for resources at carrying capacity. We set R_{max} to 0.031 and the standard deviation in growth rate to 0.05 (66) and ran the model for 1,700 years (100 generations). Population abundances were extracted at generational timesteps (i.e., year 17, 34, 51, etc.), which we then used to calculate growth rate, variance, and standard deviation at generational timesteps. This process was repeated 1,000 times before calculating the mean SD in generational growth rates (mean generation S.D. = 0.184). The upper and lower bounds for S.D. R0 were subsequently set at 0 to 0.35 accounting for allometry and uncertainty. A similar approach has been used to reconstruct variation in the growth rate of woolly mammoth (39) and muskox (38).

Dispersal

Dispersal information is lacking for the most closely related species of woolly rhinoceros. Maximum published estimates for white rhinoceros' dispersal are ~250km (69), with published estimates for comparable sized extinct megafauna ~300km (39). Due to uncertainty in estimates of maximum dispersal for extant and extinct megaherbivores, we fixed it to 500km and varied mean dispersal between 0 – 250km (Fig. S12). We varied the proportion of dispersers from 0.5 – 25% of the population within each grid-cell. Dispersal was modelled using the following equation:

$$m_{ij} = \begin{cases} p \times exp\left(\frac{-D}{b}\right), & D \le D_{max} \\ 0, & D > D_{max} \end{cases} \quad \text{Eq. 4}$$

Where movement (*m*) between cell *i* and *j* is a function of the parameters *p*, *b, D*, and D_{max} (fixed at 500km). The parameter *p* represents the proportions of dispersers, *b* represents the dispersal breadth (i.e. the average dispersal distance), and *d* represents the dispersal distance between cell *i* and *j*. This approach prevents large dispersal rates to closely neighbouring cells (i.e., the drainage effect) by pre-calculating a fixed proportion of individuals that should move to a given cell based on *p, b,* D_{max} and D_{ij}. Consequently, when mean dispersal is low and/or proportion of dispersers is low, maximum dispersal is also low.

We modelled snow limited dispersal using established relationships for other large, cold adapted but snow averse, Arctic ungulates (70). We estimated two-thirds of the chest height for a woolly rhinoceros to be 50cm, and dispersal to become more difficult when snow depths exceeded this height (17). This approach meant that dispersal between patches of suitable habitat across the landscape was more costly in areas of relatively deep snow (Fig. S18). Importantly, the relationship never decays to 0, permitting some level of dispersal even under very heavy snow. To convert snow depth to a friction layer suitable for modelling snow dispersal limitation we generated a logistic equation relating snow depth to ease of movement:

$$\text{Ease of movement} = \frac{c}{\left(1 + exp\left(\frac{e - depth}{b}\right)\right)} \quad \text{Eq. 5}$$

Where *c* is the asymptote, *e* is the depth of snow at the inflection point, and *b* equals -1/slope at the inflection point. A negative *b* value indicates that as snow depth increases, then ease of movement decreases.

Allee effect

Allee effects have previously been detected for extinct megaherbivores (71). We set a local quasi-extinction threshold (72) which made cell abundance zero if abundance fell below the Allee threshold. Due to lack of information on Allee effect for woolly rhinoceros, we slightly expanded ranges that have been predicted for woolly mammoth (39). The range of values for the Allee effect were 0 (i.e., no Allee effect) to 150 individuals per grid cell corresponding to a density of 0.015 animals/km^2 (Table S1).

Environmental correlation

This was a fixed parameter in our models that was set to *b* = 850 km where *b* is the decay constant of an exponential decline model. Our fixed parameter estimate has been used in other process-explicit macroecological models (73), including those for Eurasia during the Pleistocene-Holocene transition (38, 39). This parameter accounts for similarity in environmental fluctuations for populations located close together versus further apart.

Human harvesting

Woolly rhinoceros co-existed with Neanderthals (*Homo neanderthalensis*) and humans for long periods of time before going extinct, and there is evidence they were exploited for food in some regions(74-76). Consequently, we modelled human hunting of woolly rhinoceros as a function of the timing of the arrival and abundance of anatomically modern humans in a given grid cell (see *Human density* above), with maximum offtake rates varying from 0 – 20% of woolly rhinoceros population abundance (39) and harvesting following a Type II to a Type III functional response. We chose not to model a direct numerical response because human populations in Eurasia were not obligate hunters of woolly rhinoceros, and it is not apparent how many rhinoceroses were actively hunted and consumed by humans despite making up to 30% of their protein intake (76). Furthermore, fluctuations in human population during this time have been linked to climate and associated societal responses, including altered food-procurement strategies involving a wide variety of sources (77).

We varied exploitation of woolly rhinoceros by humans between 0 – 20% at equilibrium abundance (i.e., maximum abundance in a grid cell with HS = 1, and maximum human density). Harvesting was modelled using the following functional response:

$$\text{Functional response} = \frac{(F \times P^z)}{(G + P^z)} \qquad \text{Eq. 6}$$

Where *P* is the density of prey population (current population size, divided by maximum population size), *F* is the maximal predation rate, *G* is a constant equal to the prey density at which predation is half-maximal, and *z* is a measure of the departure from maximal predation. Functional response gives the number of prey killed per predator per year.

The harvest rate (*H*, proportion of the prey population killed) was calculated by dividing eq. 3 by the current prey density:

$$H = \frac{\left(\frac{F \times P^z}{G + P^z}\right)}{P} \qquad \text{Eq. 7}$$

The parameterisation (above) is based on considering all of the human population in a particular grid cell at maximal density as 1 predator. Thus, to get harvest rate at a particular time and grid cell, Eq. 7 was multiplied by the human population density (i.e., current human population, divided by maximum human population) at that time and grid cell:

$$H` = \frac{\left(\frac{N \times F \times P^z}{G + P^z}\right)}{P} \qquad \text{Eq. 8}$$

Where *N* is the human population density. *G* was set to 0.4 (39), and *F* varied from 0 to 0.25.

Previously Alroy (78) modelled hunting success of megafauna by setting $z = 1$ in the above equation. This resulted in a type II functional response. We modelled *z* as a variable parameter ranging from 1 to 2 (38, 39, 78). At $z = 1$ the function is monotonic, under which predation is modulated only by prey density and predator satiation, implying complete naivety of prey. At $z > 1.5$ hunting success takes on an increasingly sigmoidal Type III functional response, under which prey become harder to hunt at low densities. This might result from prey adaptation (evolved or learned behaviour), prey switching by hunters or prey being located in refugia (79, 80).

Latin Hypercube Sampling

We generated 45,000 process-explicit macroecological models using combinations of values for demographic parameters and environmental attributes based on their plausible ranges (Table S1) (39, 57). This was done using Latin Hypercube sampling and uniform distributions, providing a robust coverage of the multi-dimensional parameter space (81). Each conceivable model – with its different combinations of demographic parameter values – was run as a single replicate (39, 82) for ~51,500 years (the equivalent of 3,030 generations).

All models were initialised at carrying capacity (as defined by the relevant Latin Hypercube sample) in all areas except North America, where habitat suitability (and thus, carrying capacity) was forced to zero during model burn-in (100-generations, 1,700 years). Following burn-in, cells in North America were allowed to be colonised if habitat suitability and dispersal conditions permitted this to happen. We did this because no fossilised remains of woolly rhinoceros have been discovered on the North American side of the Beringian land bridge (19).

Pattern-oriented modelling

We used pattern-oriented modelling techniques and Approximate Bayesian Computation (ABC) (55) to determine models that did well at replicating the range dynamics of woolly rhinoceros during the late Pleistocene and Holocene. The approach provides a systematic way of assessing support for different model versions and parameterisations based on validation datasets, given some prior beliefs about how likely they are (83). Specifically, we used ABC to compare the simulated outputs against five observational targets: occurrence at fossil site at the

correct time (^{14}C age ± 1 SD); timing of regional extirpation (corrected for the Signor-Lipps effect; 84) for Europe, west Siberia, and east Siberia; and period of occurrence in North America equalling zero (19). A test of approximate sufficiency (85) suggested excluding the North American occurrence target resulted in a less informative model. We did this using the R package 'abc' (86). The summary and target statistics were treated collectively in the ABC modelling (i.e., using a multi-variate target), meaning that models were assessed on the capability to simultaneously replicate a suite of key aspects of the extinction dynamics of woolly rhinoceros.

We used the default rejection method to select models that exceeded a critical distance from the idealised targets. With the rejection method, Euclidian distances are calculated between simulated summary statistics and the validation targets. Following van der Vaart, Beaumont, Johnston and Sibly (83), we scaled the summary statistics by their standard deviations (SD), and not the median absolute deviation (MAD, the default), before calculating Euclidean distances. The SD was chosen as a scaling factor because the MAD of one summary statistic (extinction penalty of North America) was zero, leading to an undefined distance. For each round of ABC model selection, 1000 folds of cross-validation was done to choose the tolerance value that minimised the root-mean-square-error of the demographic parameters in the selected simulations (86).

We assessed the skill of an initial run of 25,000 simulations using our pattern-oriented modelling method. To further refine the parameter distributions and to improve the ability of the models to hit the validation targets, we ran an additional 10,000 simulations using informed priors. For each demographic parameter, we generated values under appropriate truncated distribution types (e.g. truncated normal, truncated negative binomial, etc.) constrained to the 90% CI of the posterior parameter distributions (i.e. the 90% CI from the selected simulations). We compared each of the informed distributions to the original posterior parameter distribution by calculating AIC values and the delta AIC (ΔAIC). Based on the distribution which provided the lowest ΔAIC for each parameter, we generated 10,000 uniformly distributed Latin-Hypercube samples, before transforming the margins of the hypercube to the desired distributions (87). These parameters were used to inform additional process-explicit models. Niches for the new runs were selected based on the range of OMI and volume of the niches selected from the ABC. In this way we avoided refining the niche to a single reconstruction, but still permitted refinement of the niche space.

After each run of simulations, we repeated the ABC validation to extract the best models. We used Bayes Factors to estimate demographic parameter convergence after each run using a 90% region of practical equivalence (88). If the prior and posterior distribution of each parameter did not converge (Bayes Factors > 1), we repeated the process of sampling new informed priors, running the simulations and validating the simulations with ABC. If the prior and posterior distributions had converged, samples were fixed at the values from the previous set of simulations. Following demographic parameter refinement and simulation, we then used ABC to compare the ability of each of all simulations from each round (i.e. not the multi-model ensemble from each round), to hit spatiotemporal fossil targets *within* each region (i.e. Europe, west Siberia, east Siberia). Analysis of Variance and post-hoc tests of significance were used to identify if each round had improved with regards to its ability to hit a more refined regional fossil target. We repeated this process a total of three times, giving a total of 45,000 simulations.

After the final round of ABC model selection, we extracted additional summary statistics to test the ability of the selected models to recreate the most recent estimates of woolly rhinoceros extinction (89). For each of the selected models (n = 100, 100, and 75 respectively for each round), we calculated the weighted distance of the final extinction event of the simulation to the last known location of woolly rhinoceros, the number of grid-cells in eastern Siberia that had populations during the revised extirpation window (9.8 ka BP ± .2 ka), and whether or not extinction in the simulation occurred after 10 ka BP. Goodness of fit tests where then done to check for differences between the ability of each simulation round to recreate the independent extinction date. Analysis of Variance and post-hoc tests of significance confirmed no difference in the ability of each round of the simulation to hit the independent validation targets (Fig. S19).

The top 100 feasible parameterisations (0.2 %) of 45,000 woolly rhinoceros–climate–human interactions were retained and used to generate weighted ensemble averaged estimates of spatial abundance, extirpation time, total population size, population fragmentation, and harvest

rates. Estimates were weighted by the inverse of the Euclidean distance of the model from the idealised targets, giving higher weights to models that best reproduced our multi-variable target.

Eemian (last interglacial) simulation

We tested whether the process-explicit model was able to reconstruct persistence of woolly rhinoceros during ancient warm events that it survived in the past. Specifically, we used the best process-driven models of woolly rhinoceros–climate–human interactions (according to POM) to simulate population abundance at the last interglacial. This involved running our model under climate and environmental conditions at 120 ka BP, according to HadCM3B-M2.1. We ran the models for 101 generations focused on 120 ka BP climate and environmental conditions with populations initiated at carrying capacity. Results of these simulations are shown as a map and a time series of abundance. The data and scripts required to run the simulations at the last interglacial are available here: https://osf.io/6F5MD/.

Counterfactual simulation

We ran a counterfactual scenario to determine the spatiotemporal role of human hunting on the range collapse and extinction of the woolly rhinoceros. To do this we set human hunting of woolly rhinoceros to zero after 21 ka BP for the best selected models. We then compared the model output with that generated from models with best estimates of harvest during this period. This allowed us to check the importance of hunting of woolly rhinoceros after the Last Glacial Maximum on its extinction dynamics.

Sensitivity analysis

Bayesian linear meta models (90) were used to test the global sensitivity of each of the demographic parameters in our process-driven simulation model. These models identified which demographic model parameters had the largest influence on minimising the Euclidian distance between simulated and inferred demographic change. We tested for main effects and two interactions: maximum density and maximum harvest, and maximum harvest and humans multiplier. These two-way interactions were included to test for additional effects of woolly rhinoceros density and the number of humans on the landscape. Models were constructed with uniform priors ($\beta_k \sim R2(0.5)$) and 10 chains, each with 50,000 samples, with the first 10,000 samples being discarded as burn-in. Model convergence was checked using Gelman-Rubin statistics. We tested for effective sample size, and visually examined trace-plots. All model diagnostics showed excellent model convergence with all parameters having Gelman-Rubin statistics of 1.0 and high effective sample sizes (mean = 437,722, S.D = 95,665). Finally, all assumptions of linear models were checked and satisfied before doing posterior predictive checks to evaluate the model predictive accuracy relative to the observed data. Posterior predictive checks showed excellent model agreement between our observed data and that generated by the Bayesian models.

Using a Bayesian sequential effect existence and significance testing framework (91) the existence, significance, and size of the effect of each parameter was then checked. We report (Table S1) the 90% CI (Highest Density Interval), along with the probability of direction (*P*(D), the probability of significance (*P*(S)), and the probability of being large (*P*(L)). The thresholds beyond which the effect is considered as significant (i.e., non-negligible) and large are |0.07| and |0.40|. These thresholds were chosen as 0.05 × SD*y* and 0.3 × SD*y* for significant and large effects, respectively (88). Where *y* is the Euclidean distance for each simulation from the idealized target.

Post simulation analysis

To determine the spatiotemporal processes and drivers that are likely to have caused the extinction of woolly rhinoceros, we discretised results from our multi-model ensemble projection of range collapse, population decline and extinction into 12 distinct glacial/interglacial periods (19, 92). For each of our fossil sites (n = 288) we identified unique grid-cells (n = 157) and extracted

continuous estimates of abundance and harvest from 60 ka BP, and reconstructions of annual average temperature, precipitation, and winter average snow-depth (7).

Spatiotemporal predictive-process generalized linear mixed effects models were then used to quantify spatiotemporal determinants of abundance. Models were fit using the sdmTMB package for R (93). Climatic variables were checked for collinearity using Kendalls Tau (τ). Temperature and precipitation values were positively correlated ($\tau > 0.7$), but there was no correlation with either variable and snow depth ($\tau = 0.08$ and 0.18, respectively). We then used generalised linear mixed models to explore the ability of temperature and precipitation to explain trends in woolly rhinoceros abundance through time. This analysis suggested that temperature had more explanatory power (Δ AIC > 3), and subsequently was used in more detailed analyses.

Due to the varying sample sizes across each of our time periods (n = 12), it was necessary to define a separate triangular analysis mesh for each period using all samples from the respective period. The mesh is used to define the spatial components in the models as random fields, with the vertices used to approximate the spatial variability in observations (93). The mesh included barriers designed to prevent the spatial effect "leaking" information across areas outside the study region (94), with the barrier defined as the maximum extent of our study region (i.e. information was contained to areas that *could* have been occupied by the simulations). In this way, our models implemented a non-stationary Gaussian random field ensuring that the spatial effects propagated with the topology of the study region (94).

Following mesh delineation, all models (n = 12) had abundance regressed against main effects of snow depth, temperature, relative harvest rates, and year of simulation, with spatially varying intercepts and coefficient estimates for snow depth, temperature, and relative harvest rates (95). We opted not to model temporal variation in the coefficients (with explicit temporal coefficients) (93) and instead to assume that the temporal response for the covariates was constant within each time period. Each model contained an additional random-walk spatiotemporal random effect to account for unobserved biotic and abiotic factors that could have been changing through time and space and were not accounted for by our covariates (e.g. vegetation change; Fig. S13). The spatial range for the spatially varying coefficients and spatiotemporal random fields components were estimated independently, using weakly informative priors (93). Models were fit with a negative binomial distribution using a half-normal non-informative prior distribution for the dispersion parameter (96, 97). Model residuals were checked for normality (Fig. S20), before spatially explicit model residuals were checked for spatial autocorrelation using Local Moran's I (98). Local Moran's I suggested there was no spatial clustering of model residuals (Fig. S21). Model performance was then assessed using the correlation between the observed and predicted abundances (Fig. S22).

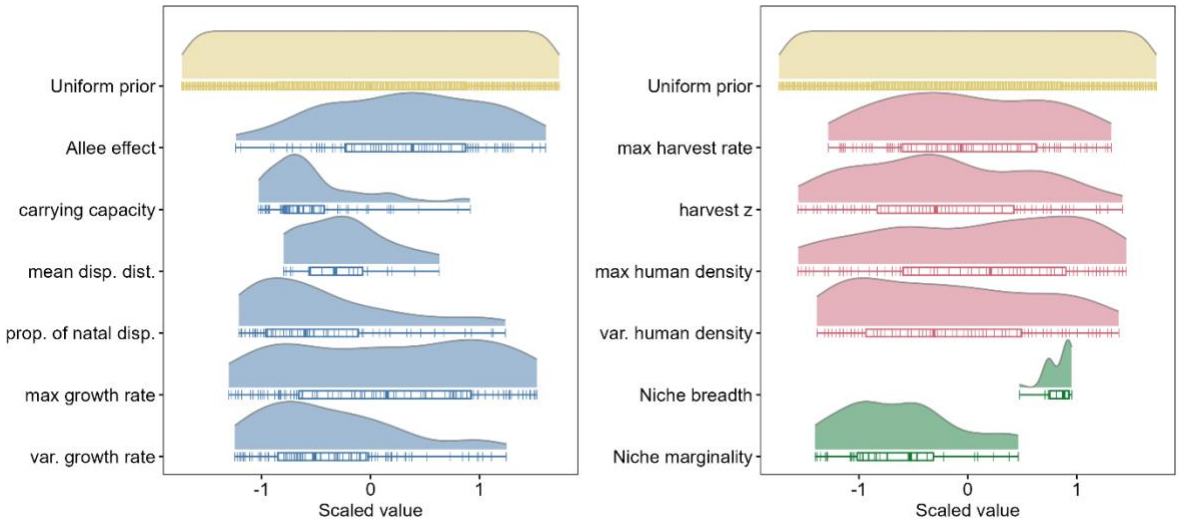

Fig. S1. Density plots of prior and posterior of model parameters. The posterior distribution from the best simulations following pattern-oriented modelling with Approximate Bayesian Computation (ABC) are shown in blue (demographic parameters), red (harvest and human abundance parameters), and green (ecological niche requirements). The uniform prior distributions are shown in yellow. Demographic parameters are Allee effect, carrying capacity, mean dispersal distance, proportion of natal dispersers, maximum (max) growth rate, and variation (Var) in growth rate. Harvest parameters were maximum harvest rate, extent to which harvest follows a Type II or Type III functional response (harvest z). Human parameters are maximum human density and variability in human density within grid-cells. Ecological niche requirements are breadth of the climatic conditions that can be occupied and their marginality, measured as the distance between average climatic conditions of the occupied and the fundamental niche. Unscaled prior and posterior values can found in Table S1.

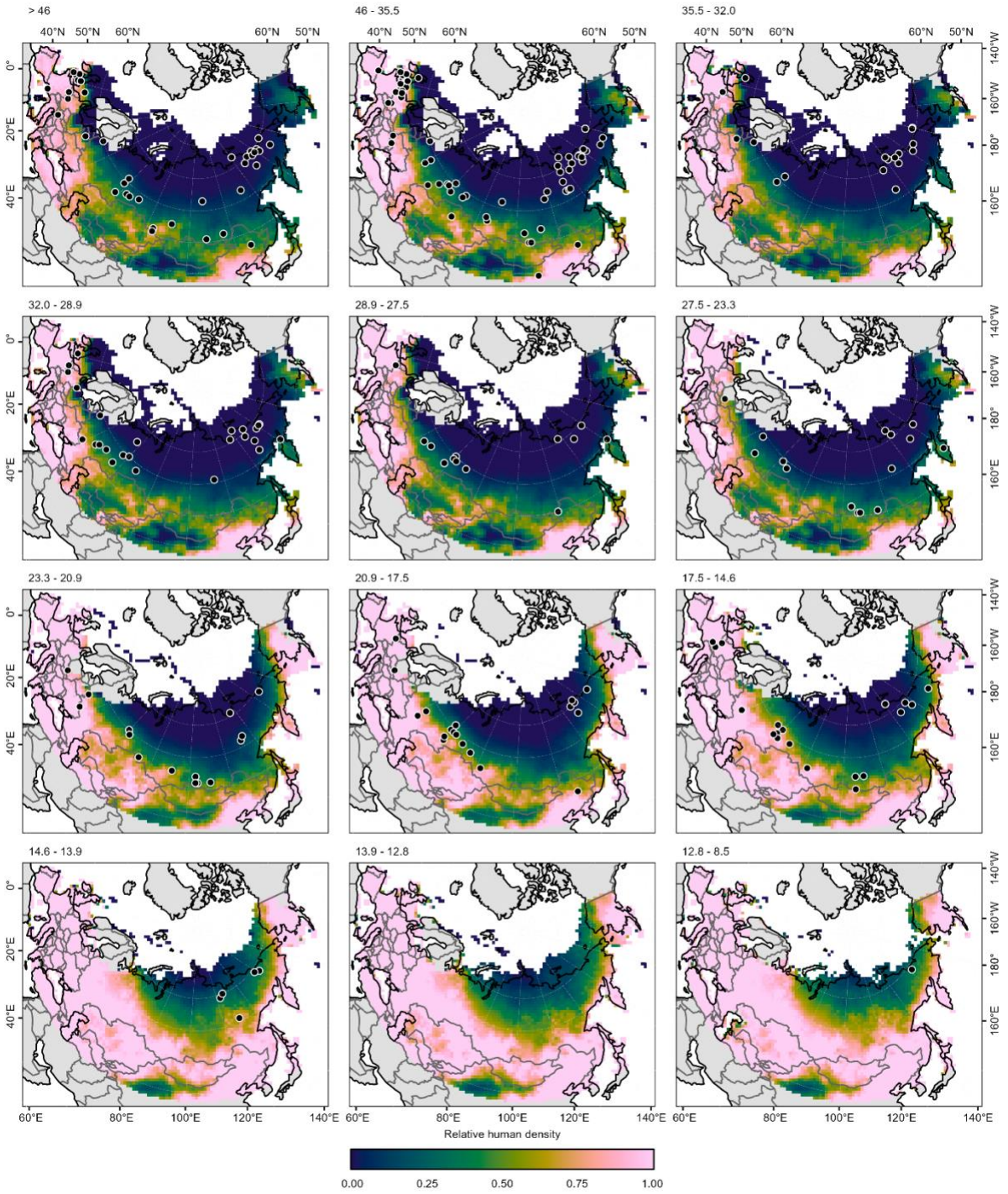

Fig. S2. Relative human density across the study region during major stadial/interstadial boundaries for process-driven model of climate-human-woolly rhinoceros interactions that validated well. Maps show the expansion and change in relative human density across the study region. Black points on the maps indicate the locations of fossils from within the corresponding time period. Densities reflect effective population size, ranging from 0 to 2126 people per 100km x 100km grid cell.

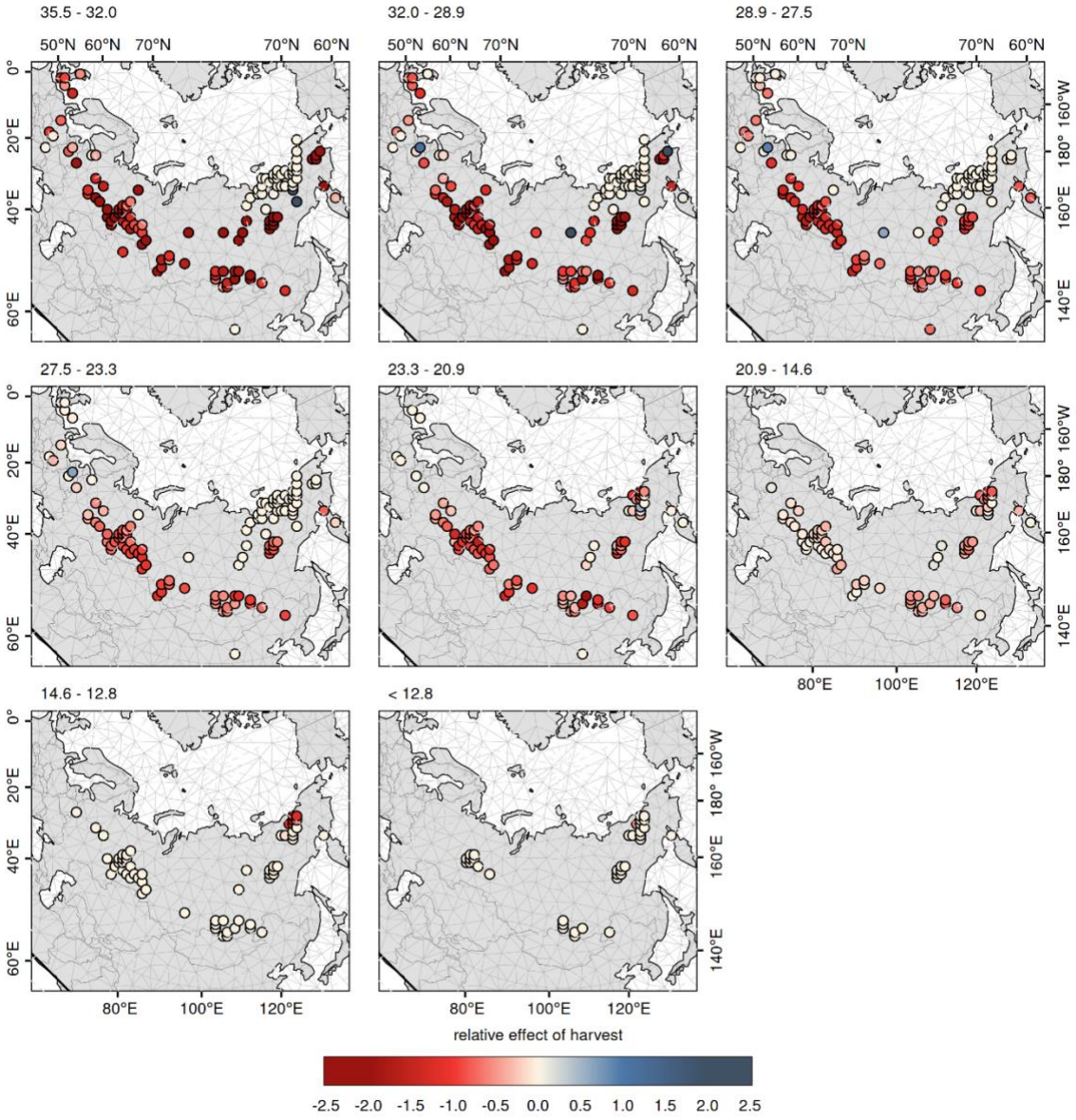

Fig. S3. Spatial effects of harvest on abundance during major stadial/interstadial boundaries. Maps show the contributing effect of relative harvest offtake on site-level abundance through space and time.

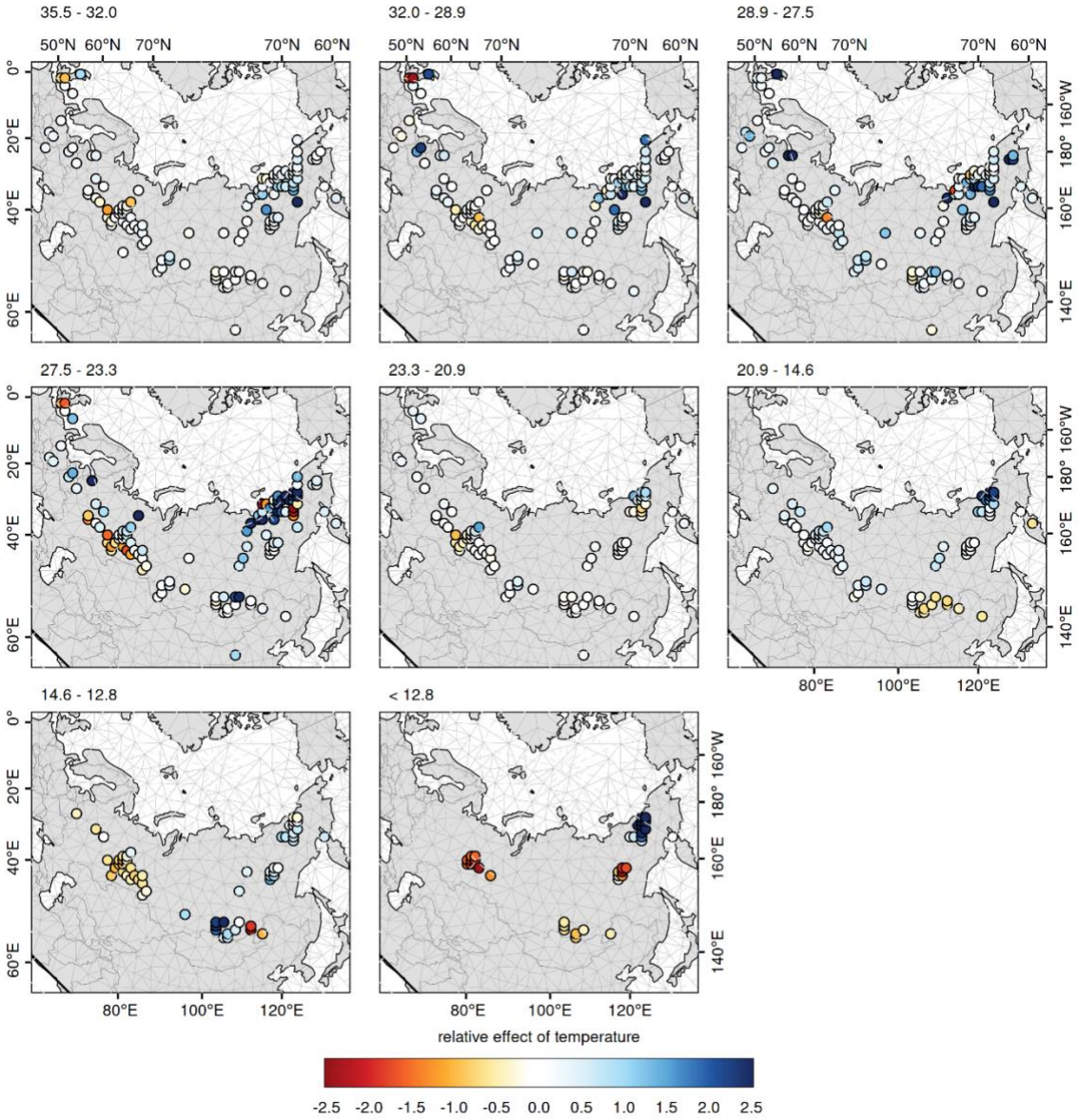

Fig. S4. Spatial effects of temperature on abundance during major stadial/interstadial boundaries. Maps show the contributing effect of changes in temperature on site-level abundance through space and time.

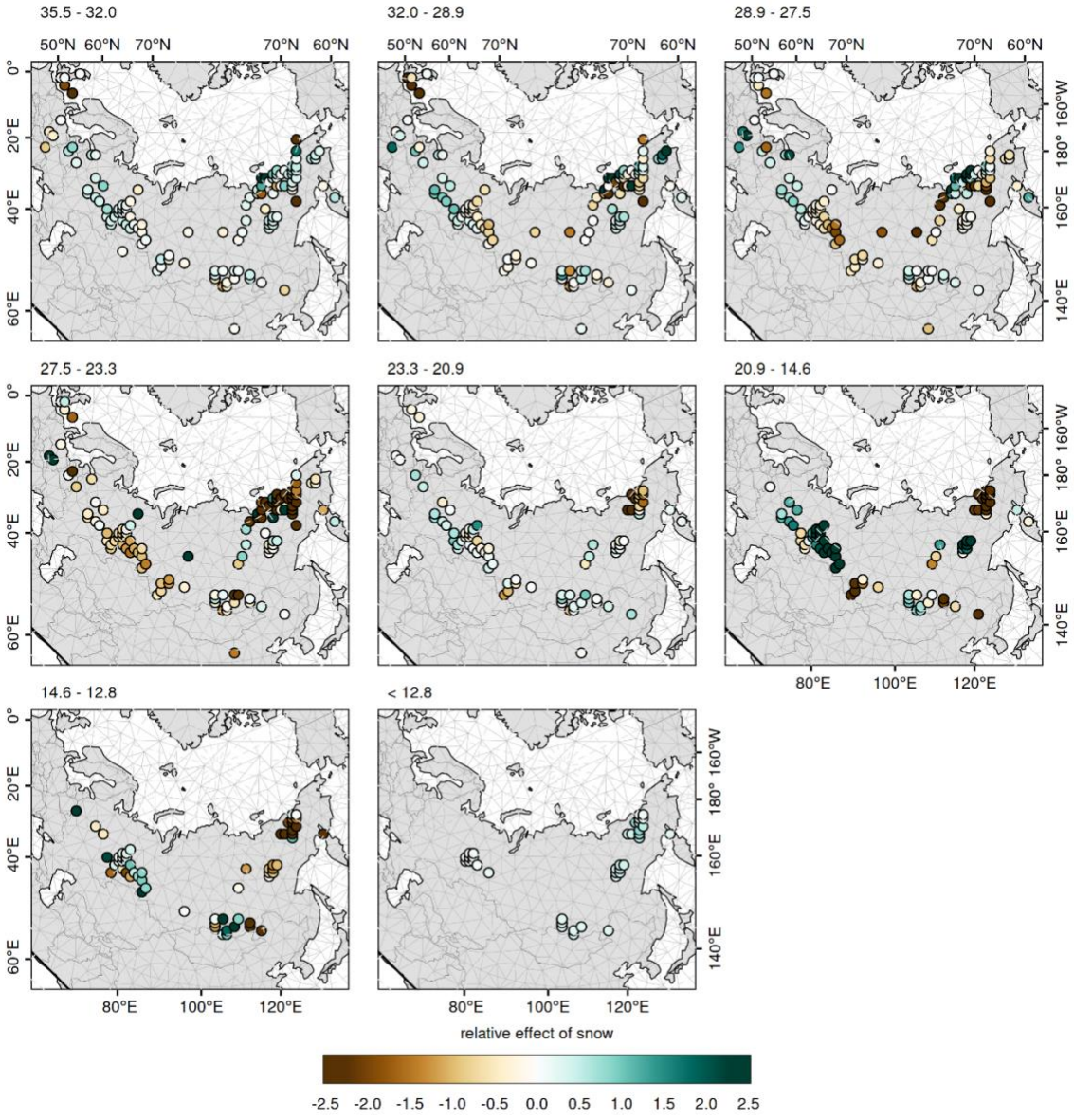

Fig. S5. Spatial effects of snow depth on abundance during major stadial/interstadial boundaries. Maps show the contributing effect of snow depth on site-level abundance through space and time. Maps of snow depth across the entire study region are shown in Fig. S7.

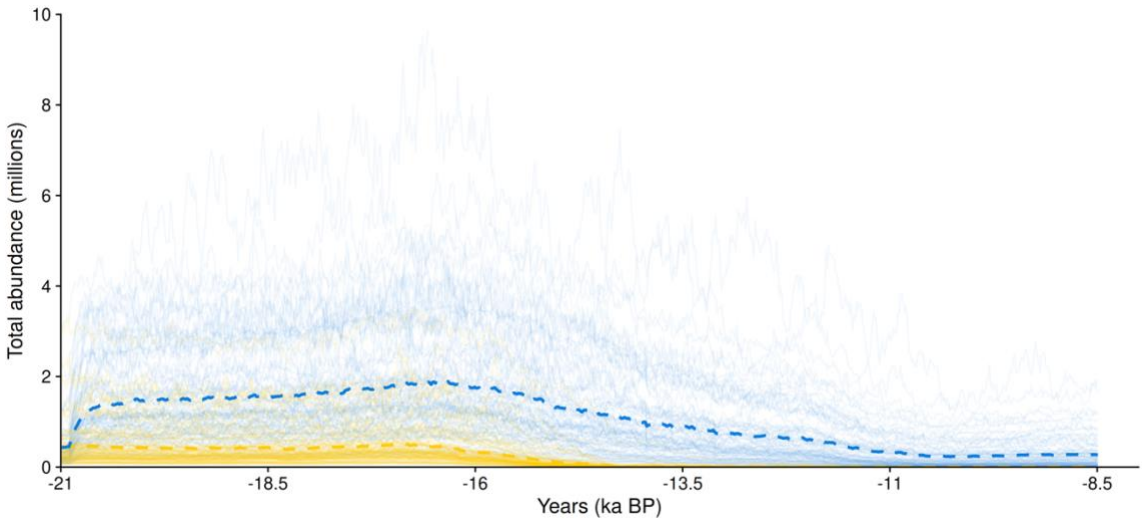

Fig. S6. Counterfactual scenario without hunting by humans. Yellow trajectories show reconstructions of population size according to the selected best 100 models. Blue trajectories show reconstructions of population size according to these same best models without hunting of woolly rhinoceroses by humans after 21 ka BP. Dashed lines show mean abundances from the selected best models.

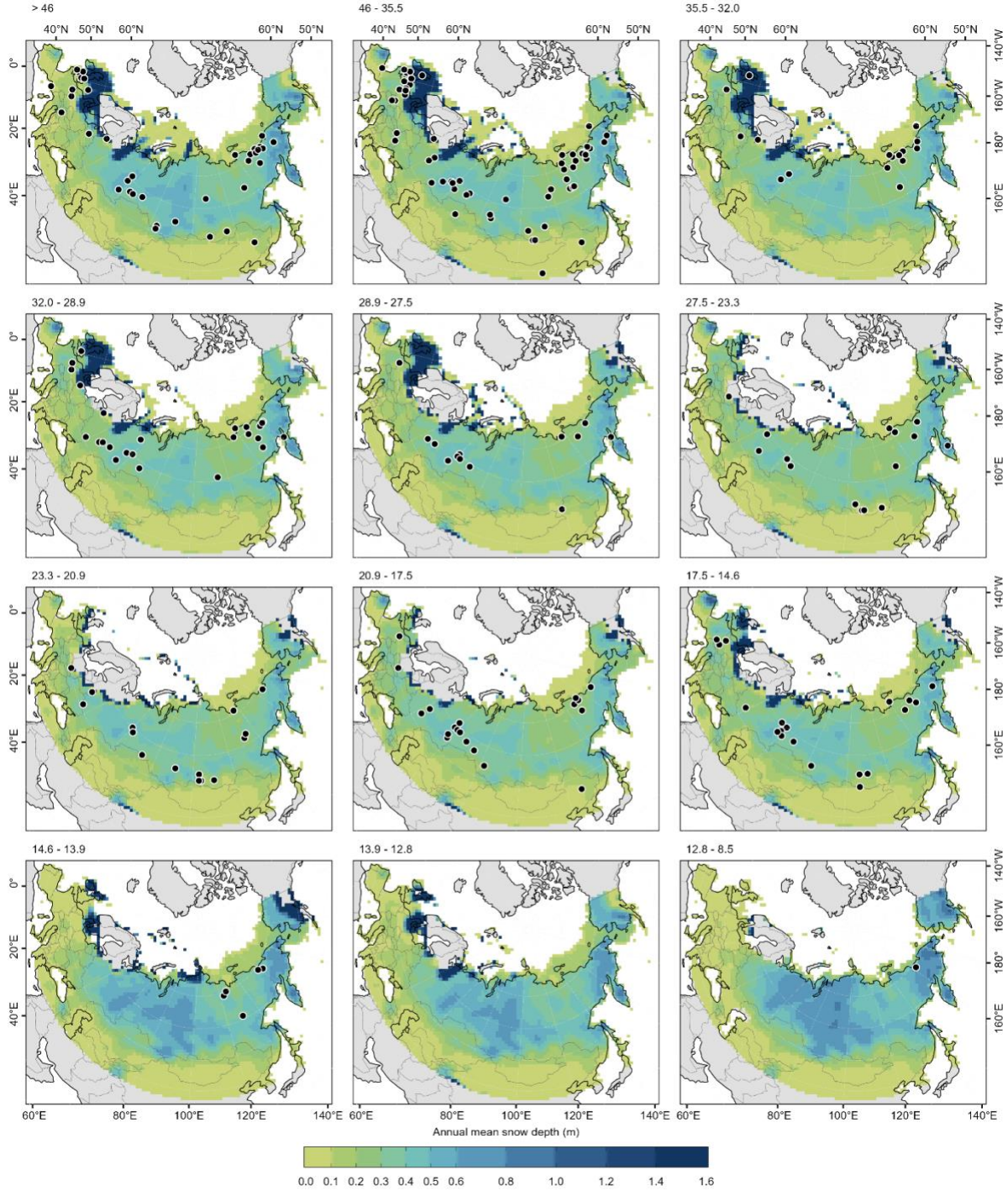

Fig. S7. Average snow depth during major stadial/interstadial boundaries. Maps show changes in the annual average snow depth (m) across the study region. The woolly rhinoceros was not adapted for dispersing through heavy snow, and after retreating to climatic refugia, populations became trapped as snow depth increased after ~17.5 ka BP. Black points on the maps indicate the locations of fossils from within the corresponding time period.

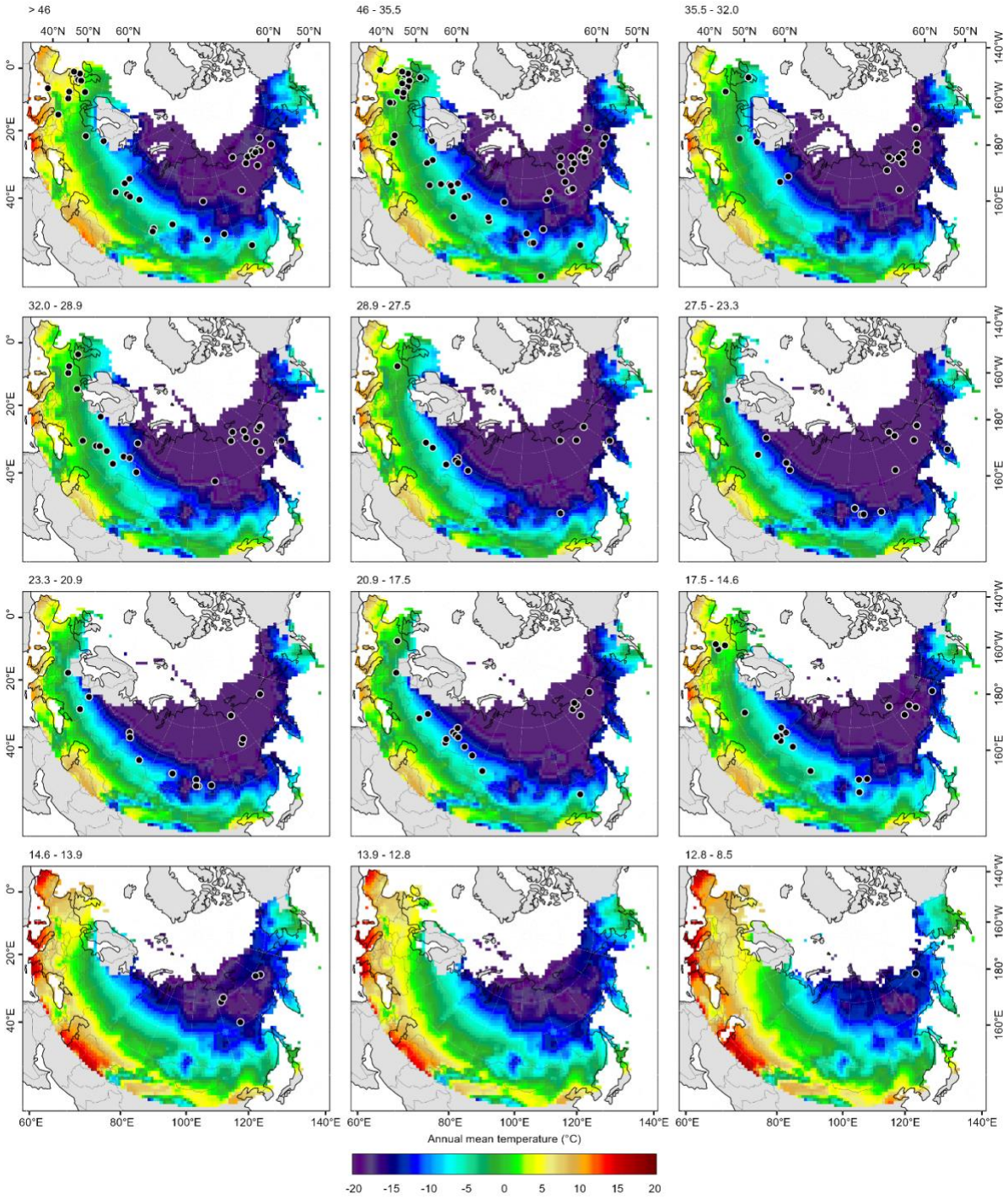

Fig. S8. Average annual temperature conditions during major stadial/interstadial boundaries. Maps show the changes in annual mean temperature across the study region. Significant warming after ~17.5 ka BP forced the woolly rhinoceros to retreat into refugia in the south of the range, and north east Siberia. Black points on the maps indicate the locations of fossils from within the corresponding time period.

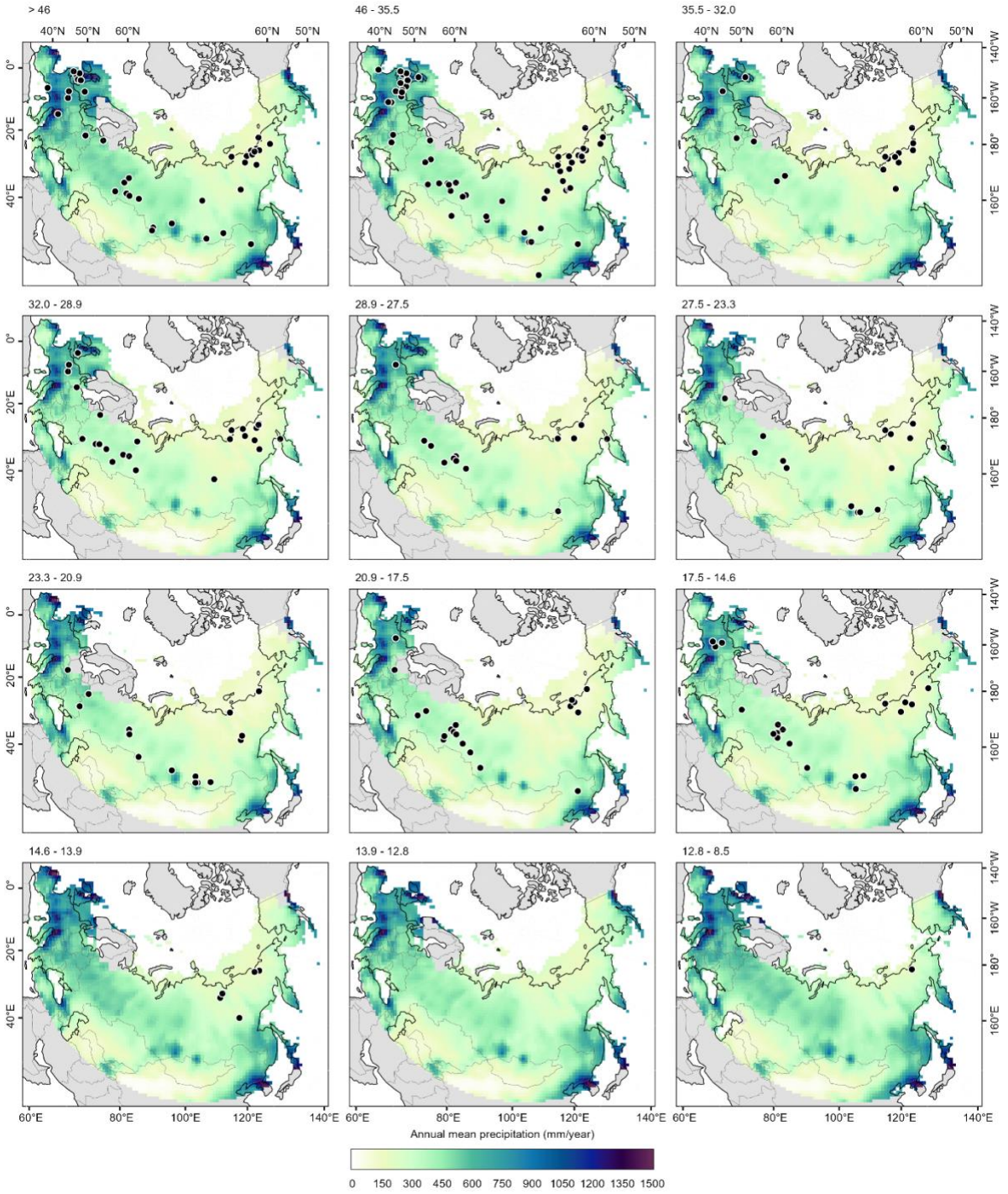

Fig. S9. Average annual total precipitation conditions during major stadial/interstadial boundaries. Maps show the changes in annual mean total precipitation across the study region. The woolly rhinoceros retreated into refugia in the south of the range, and north east Siberia as a result of drier and warmer (Fig. S8) conditions after ~17.5 ka BP. Black points on the maps indicate the locations of fossils from within the corresponding time period.

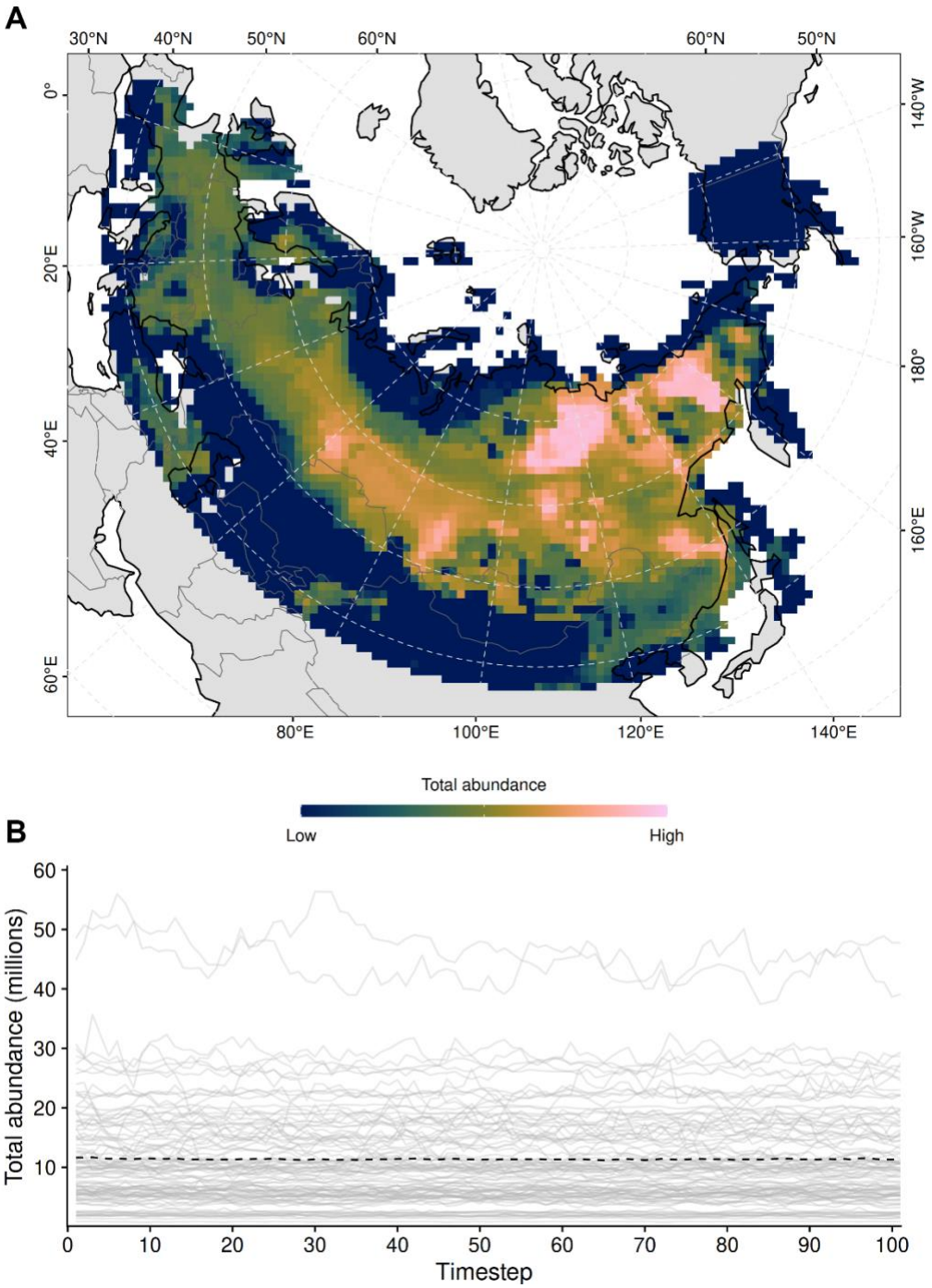

Fig S10: Map (**A**) shows the mean population abundance simulated during the Last Interglacial for the best selected models. All simulations were initialized at carrying capacity and simulated for 101 timesteps (**B**). All simulations (grey lines) had stable total abundances across the last interglacial, with mean abundance shown by the dashed black line. Each timestep represents a generation.

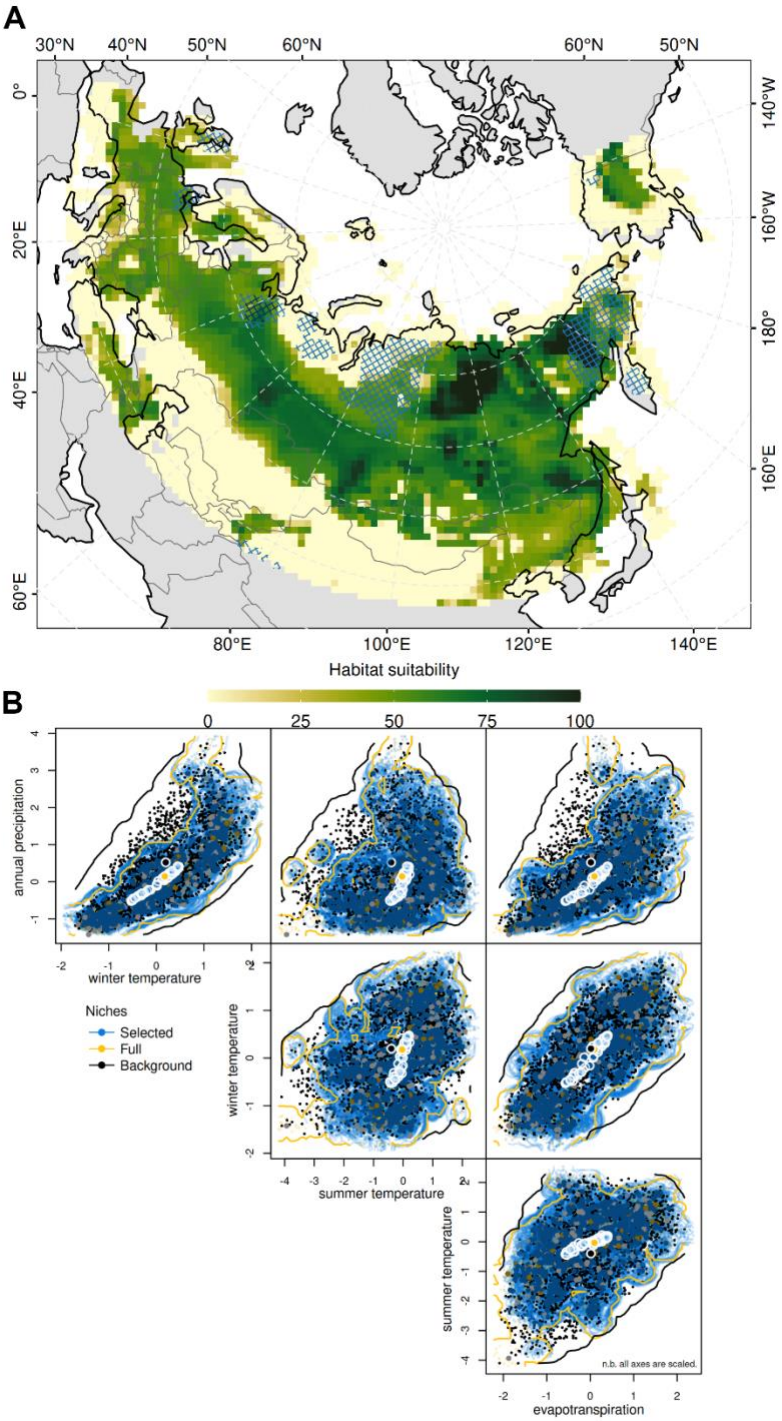

Fig. S11. Habitat suitability at the Last Interglacial**.** Map (**A**) shows the mean habitat suitability during the Last Interglacial across the selected models. Hatched areas indicate areas of moderate (0.6 – 1.5m, blue) and deep (> 1.5m, black) winter snow. The pairwise distribution of sampling points for the four climate variables used to define the niche of woolly rhinoceros (**B**). Blue points represent the selected niches, yellow the full potential climatic niche, with the black line representing the minimum convex expectation environmental background (43).

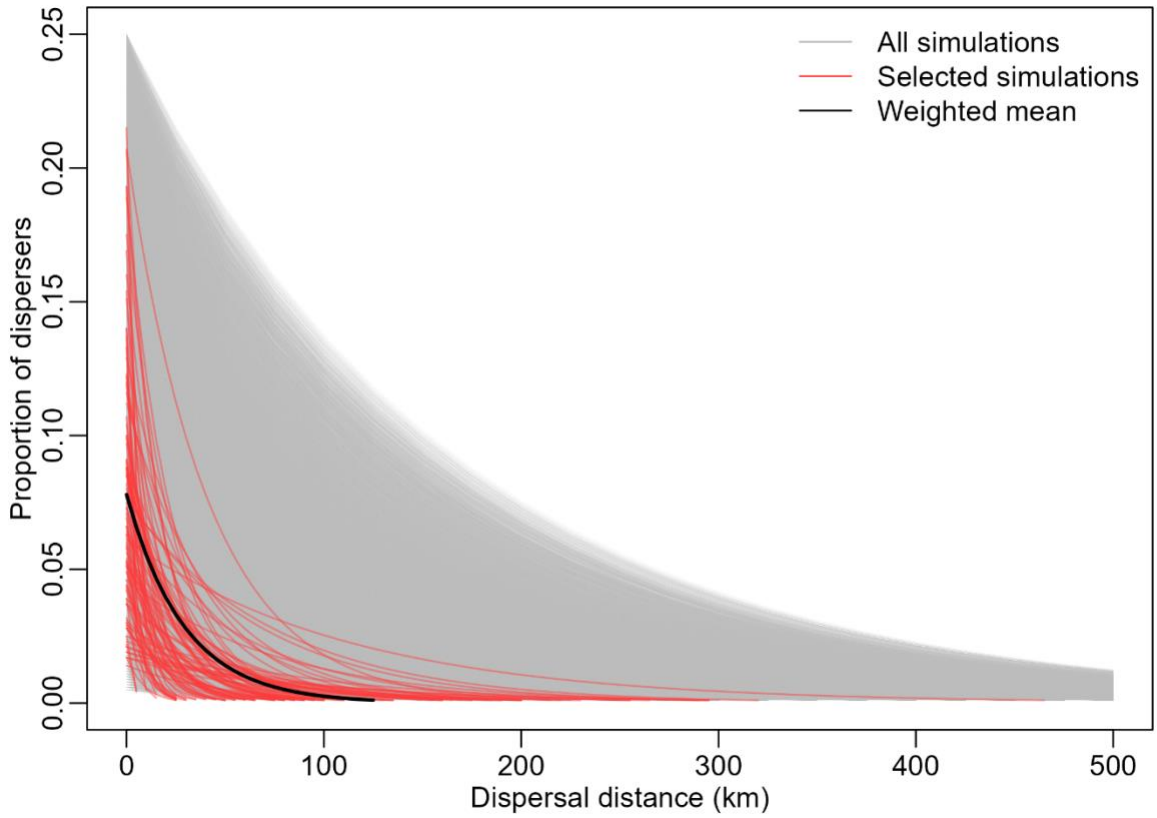

Fig. S12. Long distance dispersal function in our woolly rhinoceros–climate–human models. Lines show the exponential decay on the proportion of dispersers from each population. Grey lines show all simulations, red lines show the 100 best models, and the black line shows the ensemble weighted average dispersal.

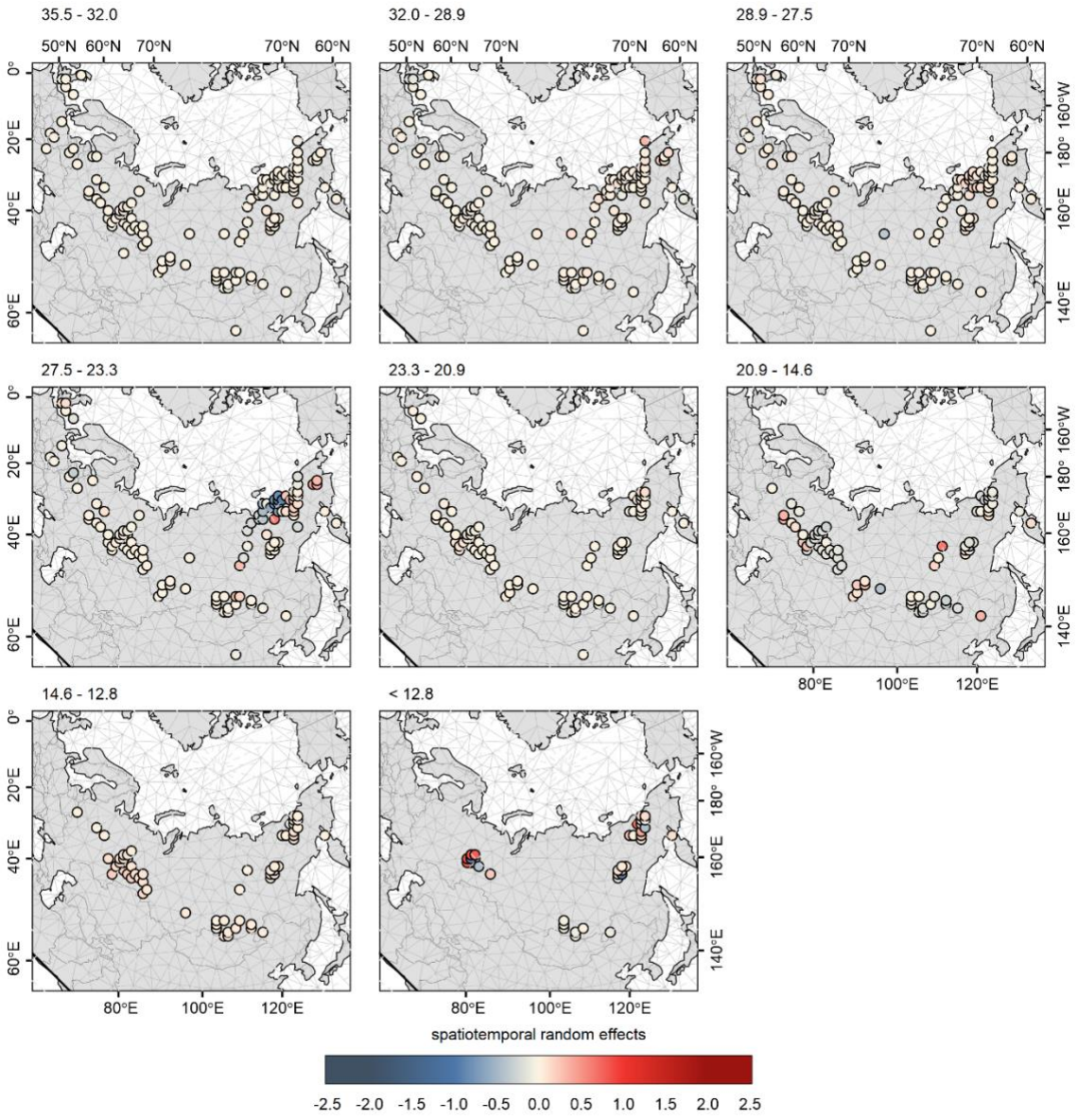

Fig. S13. Spatiotemporal random effects during major stadial/interstadial periods. These represent biotic and abiotic factors that are changing through time and space and are not accounted for in our predictive-process models (e.g. vegetation change).

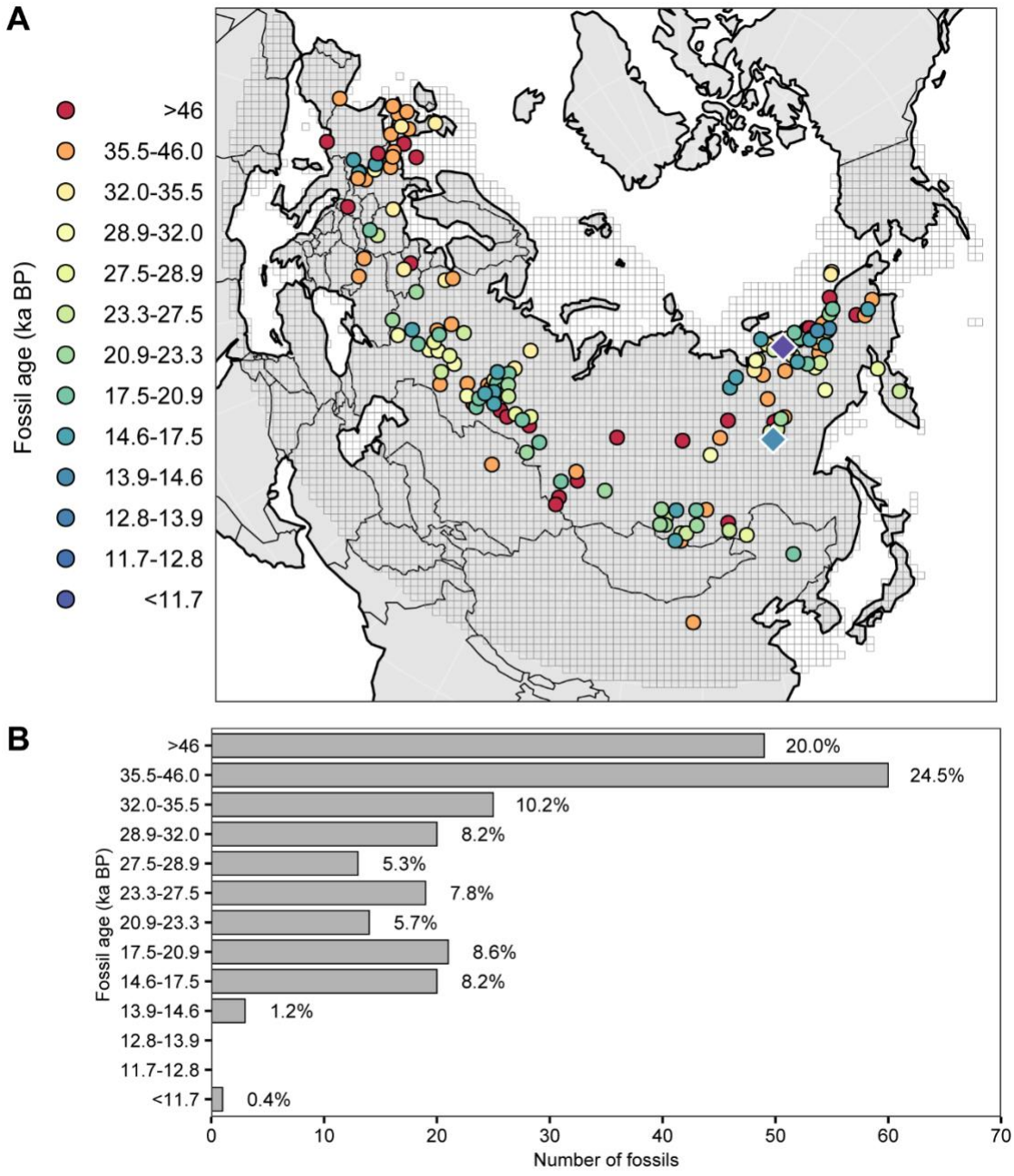

Fig. S14. Location of the study site, fossil locations, and radiocarbon dates across Eurasia. (**A**) Map shows the location of radiocarbon dated fossils records for *C. antiquitatis*, along with the median calibrated age of the fossil (**A**). The blue diamond in east Siberia shows the final extinction location as estimated by the fossil record. The purple diamond in north-east Siberia shows the location of the final extinction as estimated from aDNA (9.8 ka BP ± .2 ka BP; 89). Barplot shows the number of samples within major stadial and interstadial boundaries (92), with percentages showing the %-contribution of each time bin to the full fossil record (**B**). Note that the sample from <11.7 ka BP is from sedimentary aDNA (89).

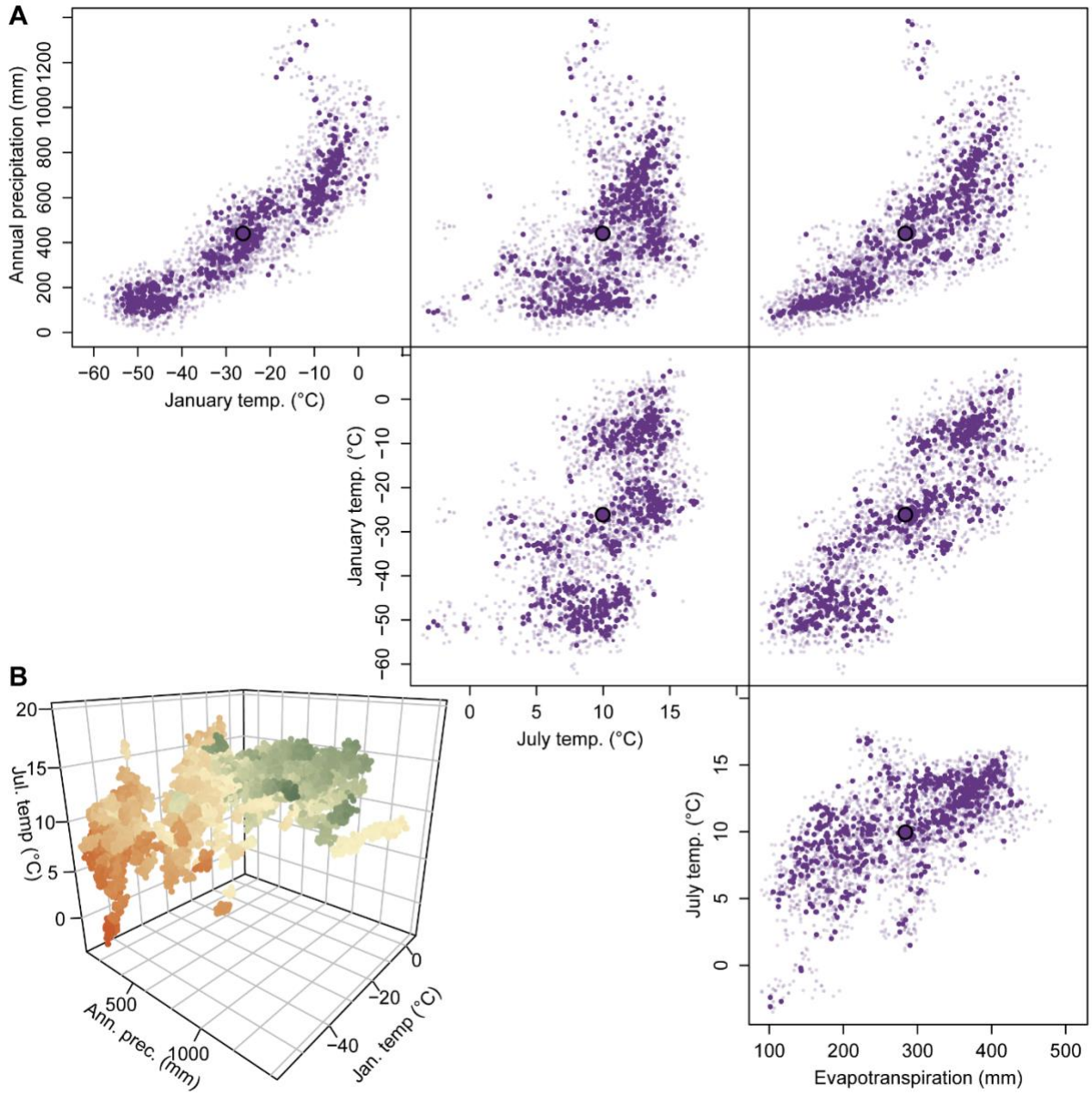

Fig. S15. The four-dimensional multi-temporal “fundamental” niche hypervolume generated for woolly rhinoceros across Eurasia. The pairwise distribution of sampling points for the four climate variables used to define the fundamental niche of woolly rhinoceros (**A**). Dark purple points represent conditions at fossil sites, with light purple points representing background points. 3D plot of the environmental space woolly rhinoceros occupied for the n = 244 fossil records, with points coloured by fossil age with points coloured by evapotranspiration (**B**). Points are sampled across the temporal span of each fossil (mean age ± 1 SD). Green = high evapotranspiration, red = low evapotranspiration.

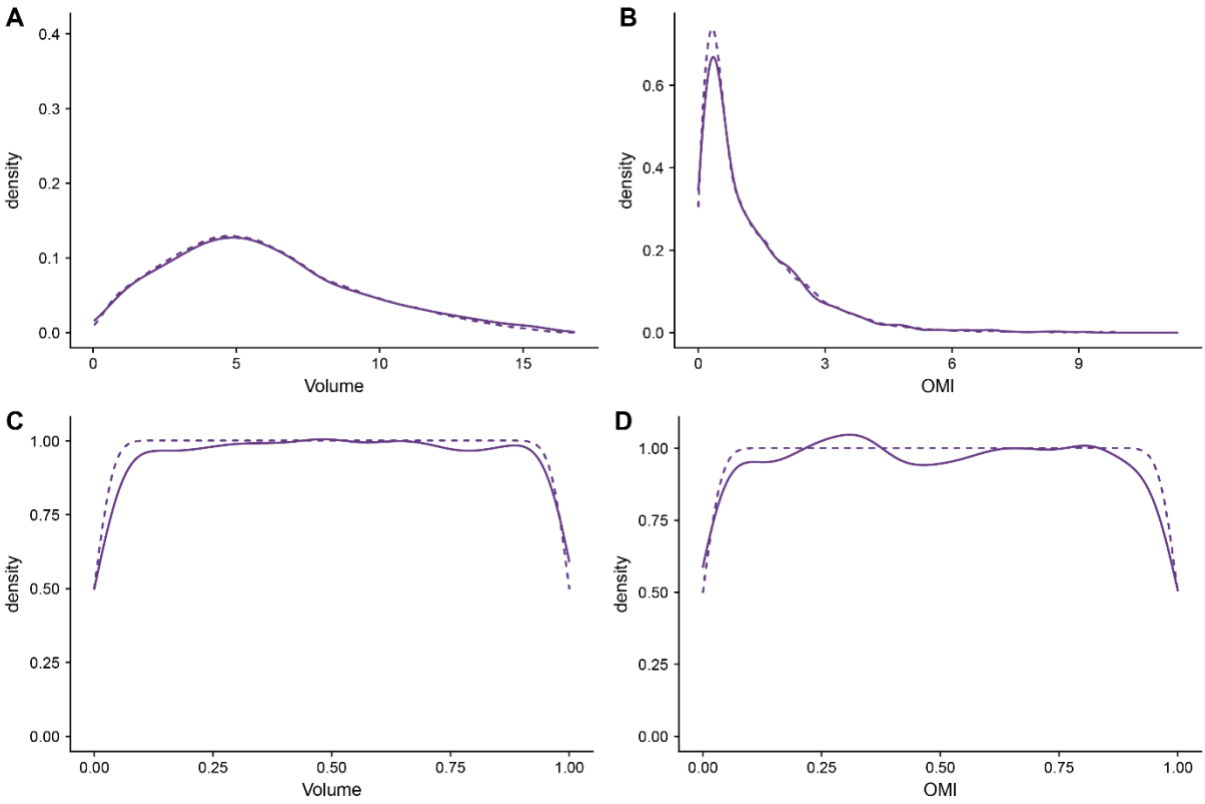

Fig. S16. Results of subsampling the niche cuts for woolly rhinoceros. The original hypervolume volume (breadth) (**A**) and OMI (marginality) measurements (**B**), and the values once transformed to uniform distributions (**C-D**). Values for all niche cuts are shown by the dotted lines in **A-D**; solid lines show the distribution of the 3,000 subsampled niche cuts.

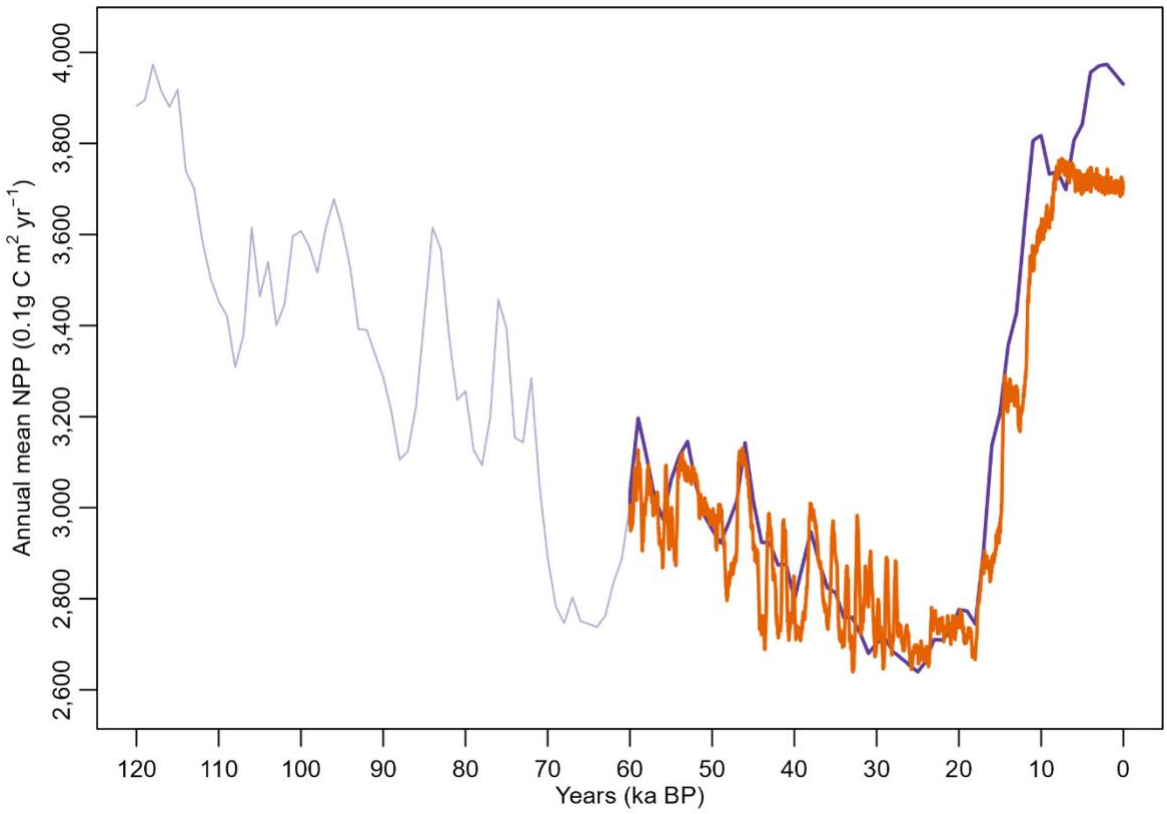

Fig. S17. Annual mean global net primary productivity used by CISGeM. The light purple line shows the previous NPP reconstruction used by (51). Following (54), we blended a higher temporal resolution NPP construction (7) (orange line), for the period 60ka – 0 BP. The Armstrong, Hopcroft and Valdes (7) data was blended to the original reconstruction using a multiplicative bias correction to prevent any step changes. The original NPP data for the period 60 ka – 0 BP is shown by the dark purple line. Whilst generational variability in NPP is much higher in our dataset, the values are of a similar magnitude.

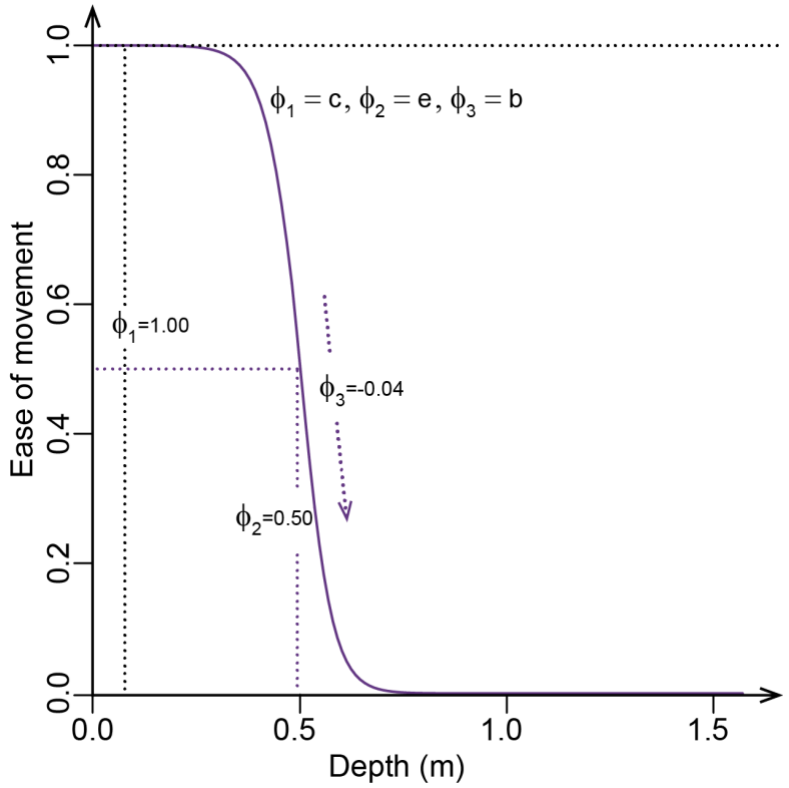

Fig. S18. The logistic curve relating snow depth to ease of movement for dispersal. As snow depth increased, the cost of movement rapidly increased following a critical depth. Importantly, the ease of movement never reaches zero permitting some level of dispersal even under adverse conditions.

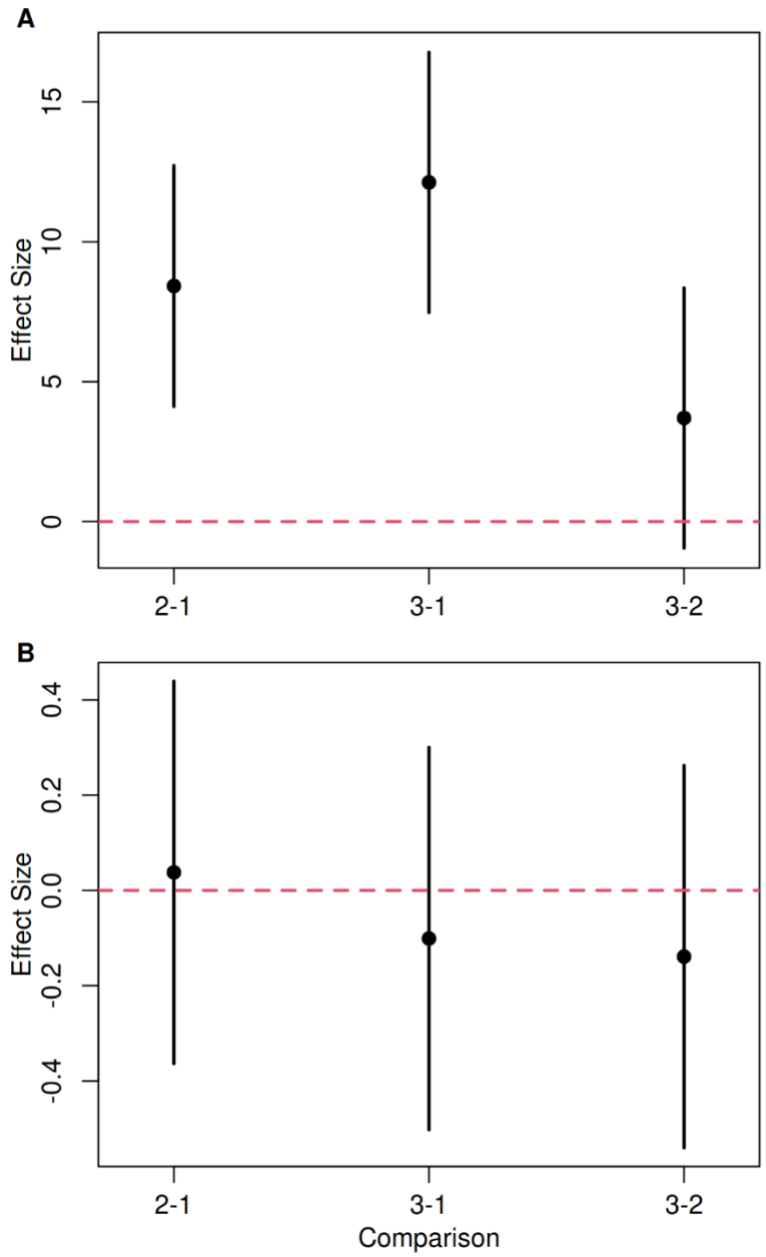

Fig. S19. Post-hoc testing for multiple simulation rounds. Post-hoc testing suggested significant differences between simulation round 1 to additional rounds of simulation with large differences in the ability to hit the number of fossils (%) within each region (A). However, there was no difference between rounds 2 and 3 suggesting convergence. Further testing on independent validation data showed that all three simulation rounds were able to effectively recreate the extirpation pattern from estimates of aDNA (16), with no significant pairwise differences (B).

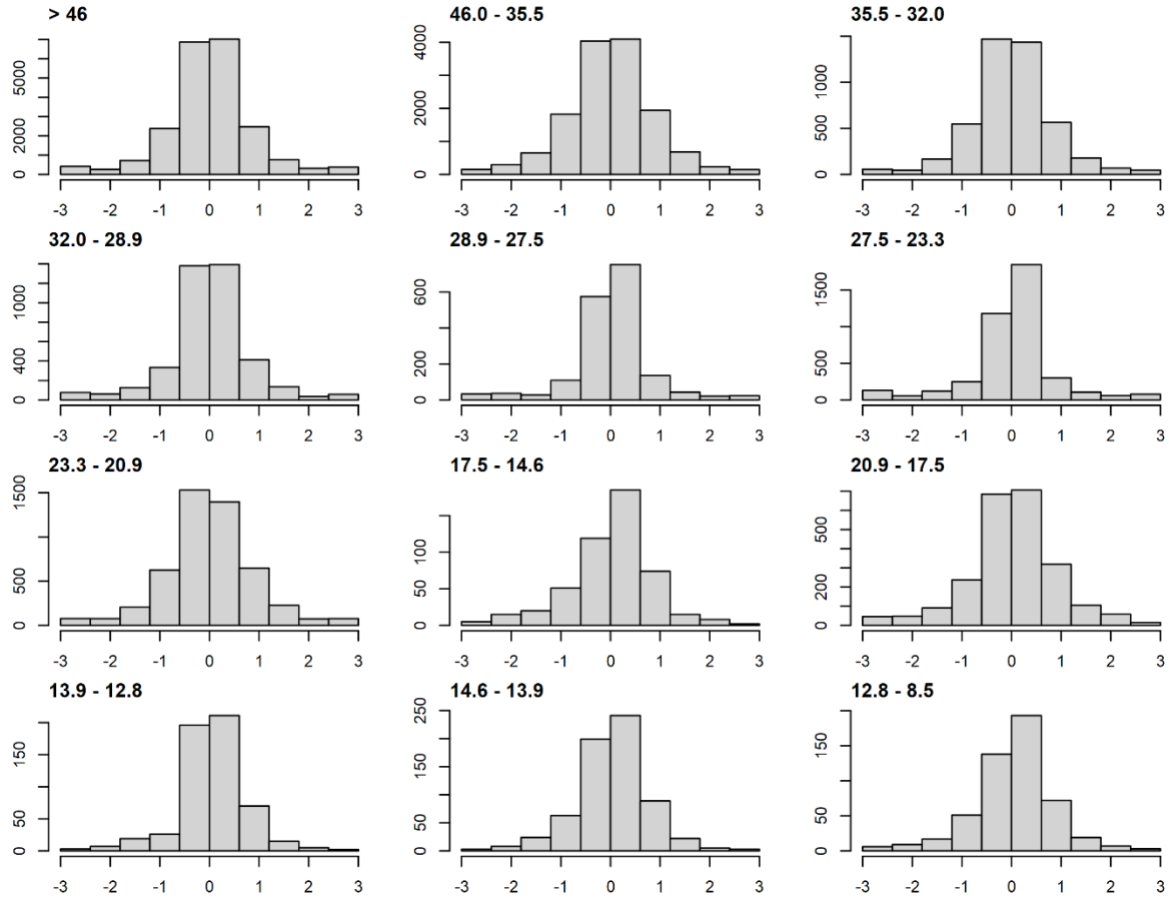

Fig. S20. Histograms of standardised model residuals for each time period. Model residuals were normally distributed suggesting correct model specification.

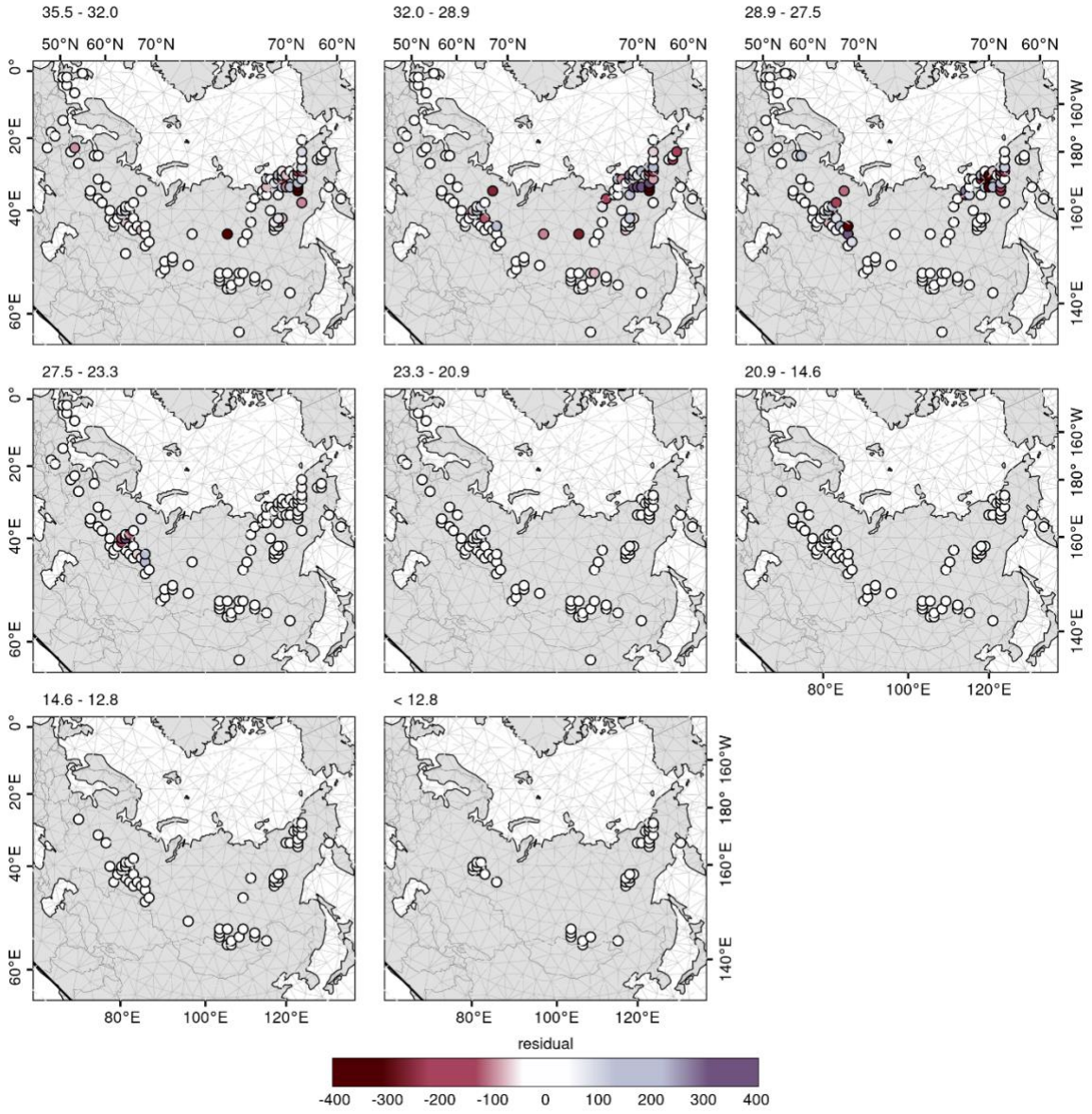

Fig. S21. Spatially explicit model residuals from our spatiotemporal GLMM's. Local indicator of spatial autocorrelation suggested there was no clustering of model residuals.

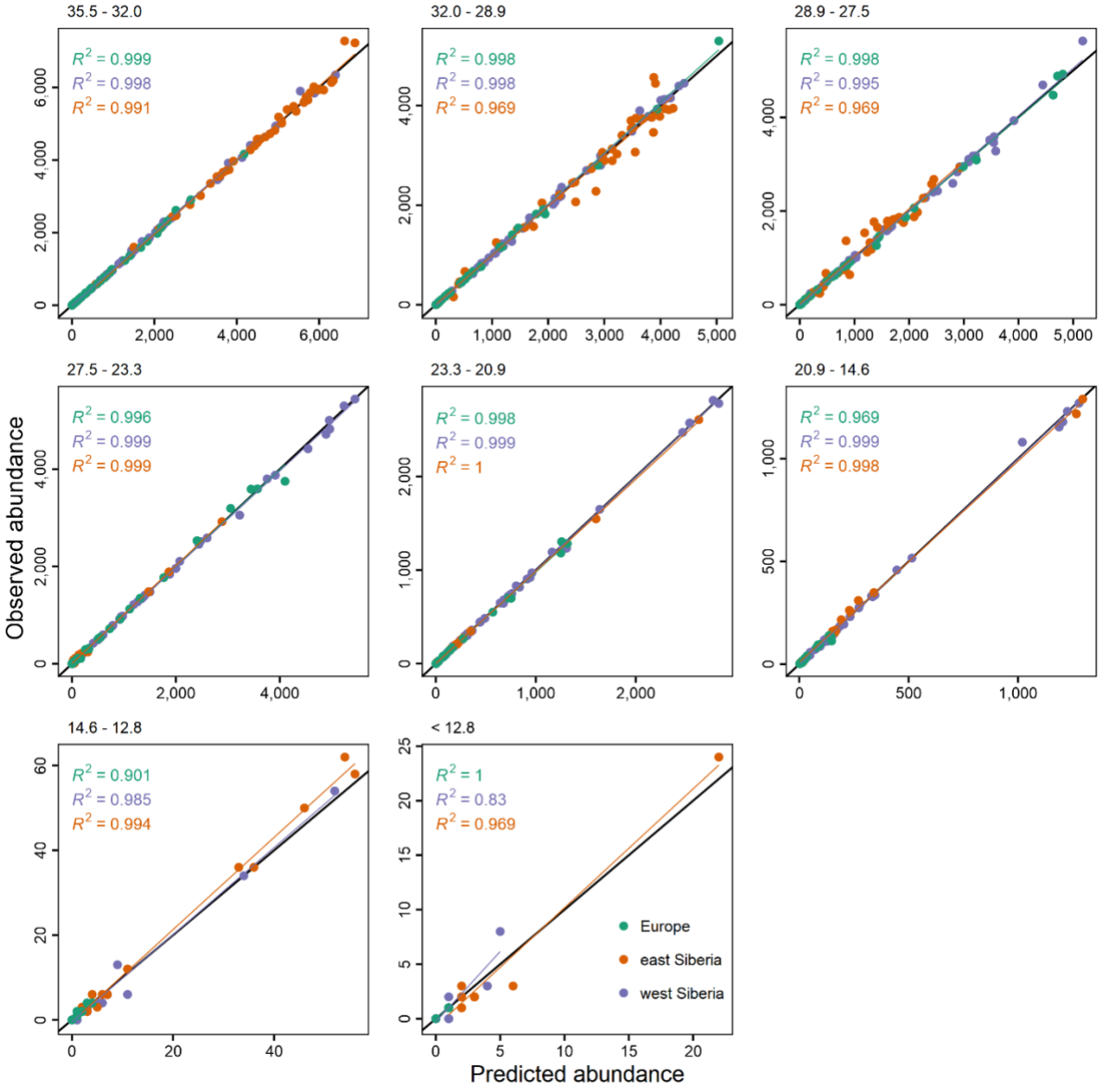

Fig. S22. Predicted versus observed abundances for each time period from our spatiotemporal GLMM's. Model performance was excellent across each of our time periods.

Table S1. Prior and posterior ranges for the best selected models. Prior ranges were chosen to represent wide, but plausible parameter ranges based on estimates from the literature. Posterior ranges are minimum and maximum values from the 100 best selected simulations. Posterior means are weighted means based on distances from idealized targets. BF = Bayes factors. BF greater than 1 suggest the posteriors are significantly different from the priors. BF indicates that posterior distributions for the final round of simulations had converged for all but two parameters, suggesting no difference in posterior values for simulation round 2 and 3, and that further refinement would likely result in overfitting (38). 90% CI = 90% confidence interval (from the posterior highest density interval) of the parameter estimate from the Bayesian meta-model. *P*(D), *P*(S), and *P*(L) are the probability of the effect of a given variable being constrained to the direction (D) of the parameter estimate, the size (S) of the parameter effect, and if the effect is large (L) (91)

Parameter	Prior range	Post. range	Post. mean	BF	90% CI	*P*(D)	*P*(S)	*P*(L)
Allee effect	10, 150	30, 145	93	1.100	0.03, 0.09	1.00	0.46	0.00
Carrying capacity	75, 32,500	1,300, 30,000	9,500	0.307	-0.24, -0.18	1.00	1.00	0.00
Mean dispersal distance (km)	0, 250	3, 114	30	0.047	0.06, 0.13	1.00	0.93	0.00
Proportion of natal dispersers	0.005, 0.25	0.01, 0.22	0.08	0.611	0.03, 0.09	1.00	0.34	0.00
Maximum growth rate	0.00, 0.69	0.09, 0.65	0.38	0.617	-0.57, -0.52	1.00	1.00	1.00
Variability in growth rate	0.00, 0.30	0.02, 0.27	0.11	0.979	0.12, 0.17	1.00	1.00	0.00
Maximum harvest rate	0.00, 0.20	0.03, 0.18	0.10	1.050	0.37, 0.44	1.00	1.00	0.58
Harvest z	1.00, 2.00	1.05, 1.91	1.43	0.610	-0.69, -0.63	1.00	1.00	1.00
Maximum human density	0.00, 1.00	0.05, 0.92	0.53	0.635	-0.17, -0.12	1.00	1.00	0.00
Variability in human density	0.00, 1.00	0.10, 0.90	0.45	0.524	0.43, 0.48	1.00	1.00	1.00
Niche breadth	0.00, 1.00	0.65, 1.00	0.88	N/A	-1.30, -1.22	1.00	1.00	1.00
Niche marginality	0.00, 1.00	0.01, 0.64	0.25	N/A	0.50, 0.57	1.00	1.00	1.00

Movie S1 (separate file). Estimates of relative abundance of woolly rhinoceros from the best selected simulations. Red diamonds show location and timing of radiocarbon dated fossils with high-quality dates.

Movie S2 (separate file). Weighted average habitat suitability from the best selected simulations. Red diamonds show location and timing of radiocarbon dated fossils with high-quality dates.

Dataset S1 (separate file). Fossil database for woolly rhinoceros, including metadata.

Software S1 (separate file). Code and data necessary to reproduce the best selected simulations**:** https://osf.io/6F5MD/

SI References

1. Andrew Martindale, *et al.*: Canadian Archaeological Radiocarbon Database (CARD 2.1). https://www.canadianarchaeology.ca/help
2. van Andel TH (2017) The Climate and Landscape of the Middle Part of the Weichselian Glaciation in Europe: The Stage 3 Project. *Quaternary Research* 57(1):2-8. 10.1006/qres.2001.2294.
3. Barnosky AD & Lindsey EL (2010) Timing of Quaternary megafaunal extinction in South America in relation to human arrival and climate change. *Quaternary International* 217(1-2):10-29. 10.1016/j.quaint.2009.11.017.
4. Bronk Ramsey C (2016) Bayesian Analysis of Radiocarbon Dates. *Radiocarbon* 51(1):337-360. 10.1017/s0033822200033865.
5. Reimer PJ, *et al.* (2013) Intcal13 and Marine13 Radiocarbon Age Calibration Curves 0-50,000 Years Cal BP. *Radiocarbon* 55(4):1869-1887. 10.2458/azu_js_rc.55.16947.
6. Faurby S & Araujo MB (2018) Anthropogenic range contractions bias species climate change forecasts. *Nature Climate Change* 8(3):252-+. 10.1038/s41558-018-0089-x.
7. Armstrong E, Hopcroft PO, & Valdes PJ (2019) A simulated Northern Hemisphere terrestrial climate dataset for the past 60,000 years. *Sci Data* 6(1):265. 10.1038/s41597-019-0277-1.
8. Valdes PJ, *et al.* (2017) The BRIDGE HadCM3 family of climate models: HadCM3@Bristol v1.0. *Geoscientific Model Development* 10(10):3715-3743. 10.5194/gmd-10-3715-2017.
9. Dansgaard W, *et al.* (1993) Evidence for General Instability of Past Climate from a 250-Kyr Ice-Core Record. *Nature* 364(6434):218-220. 10.1038/364218a0.
10. Heinrich H (1988) Origin and Consequences of Cyclic Ice Rafting in the Northeast Atlantic-Ocean during the Past 130,000 Years. *Quaternary Research* 29(2):142-152. 10.1016/0033-5894(88)90057-9.
11. Peltier WR (2004) Global Glacial Isostasy and the Surface of the Ice-Age Earth: The ICE-5G (VM2) Model and GRACE. *Annual Review of Earth and Planetary Sciences* 32(1):111-149. 10.1146/annurev.earth.32.082503.144359.
12. Kapsch M-L, Mikolajewicz U, Ziemen F, & Schannwell C (2022) Ocean Response in Transient Simulations of the Last Deglaciation Dominated by Underlying Ice-Sheet Reconstruction and Method of Meltwater Distribution. *Geophysical Research Letters* 49(3):e2021GL096767. 10.1029/2021GL096767.
13. Liu Z, *et al.* (2009) Transient Simulation of Last Deglaciation with a New Mechanism for Bølling-Allerød Warming. *Science* 325(5938):310-314. doi:10.1126/science.1171041.
14. Huntley B, *et al.* (2023) Global biome patterns of the Middle and Late Pleistocene. *Journal of Biogeography* 50(8):1352-1372. 10.1111/jbi.14619.
15. Lorenzen ED, *et al.* (2011) Species-specific responses of Late Quaternary megafauna to climate and humans. *Nature* 479(7373):359-364. 10.1038/nature10574.
16. Nogues-Bravo D, Ohlemuller R, Batra P, & Araujo MB (2010) Climate predictors of late quaternary extinctions. *Evolution* 64(8):2442-2449. 10.1111/j.1558-5646.2010.01009.x.

17. Boeskorov GG (2012) Some specific morphological and ecological features of the fossil woolly rhinoceros (Coelodonta antiquitatis Blumenbach 1799). *Biology Bulletin* 39(8):692-707. 10.1134/S106235901208002X.
18. Stefaniak K*, et al.* (2021) Browsers, grazers or mix-feeders? Study of the diet of extinct Pleistocene Eurasian forest rhinoceros Stephanorhinus kirchbergensis (Jäger, 1839) and woolly rhinoceros Coelodonta antiquitatis (Blumenbach, 1799). *Quaternary International* 605-606:192-212. 10.1016/j.quaint.2020.08.039.
19. Stuart AJ & Lister AM (2012) Extinction chronology of the woolly rhinoceros Coelodonta antiquitatis in the context of late Quaternary megafaunal extinctions in northern Eurasia. *Quaternary Science Reviews* 51:1-17. 10.1016/j.quascirev.2012.06.007.
20. Rosenzweig ML (1968) Net Primary Productivity of Terrestrial Communities - Prediction from Climatological Data. *American Naturalist* 102(923p):67-+. 10.1086/282523.
21. Compo GP*, et al.* (2011) The Twentieth Century Reanalysis Project. *Quarterly Journal of the Royal Meteorological Society* 137(654):1-28. 10.1002/qj.776.
22. Rey-Iglesia A*, et al.* (2021) Late Pleistocene paleoecology and phylogeography of woolly rhinoceroses. *Quaternary Science Reviews* 263:106993. 10.1016/j.quascirev.2021.106993.
23. Guthrie RD (2006) New carbon dates link climatic change with human colonization and Pleistocene extinctions. *Nature* 441(7090):207-209. 10.1038/nature04604.
24. Franzmann AW & Schwartz CC (1997) *Ecology and management of the North American moose* (Smithsonian Institution Press).
25. Gilbert SL, Hundertmark KJ, Person DK, Lindberg MS, & Boyce MS (2017) Behavioral plasticity in a variable environment: snow depth and habitat interactions drive deer movement in winter. *Journal of Mammalogy* 98(1):246-259. 10.1093/jmammal/gyw167.
26. Stuart AJ (2015) Late Quaternary megafaunal extinctions on the continents: a short review. *Geological Journal* 50(3):338-363. 10.1002/gj.2633.
27. Piao SL*, et al.* (2011) Changes in satellite-derived vegetation growth trend in temperate and boreal Eurasia from 1982 to 2006. *Global Change Biology* 17(10):3228-3239. 10.1111/j.1365-2486.2011.02419.x.
28. Verbyla D & Kurkowski TA (2019) NDVI-Climate relationships in high-latitude mountains of Alaska and Yukon Territory. *Arctic Antarctic and Alpine Research* 51(1):397-411. 10.1080/15230430.2019.1650542.
29. Brümmer C*, et al.* (2012) How climate and vegetation type influence evapotranspiration and water use efficiency in Canadian forest, peatland and grassland ecosystems. *Agricultural and Forest Meteorology* 153:14-30. 10.1016/j.agrformet.2011.04.008.
30. Vicente-Serrano SM*, et al.* (2014) Reference evapotranspiration variability and trends in Spain, 1961-2011. *Global and Planetary Change* 121:26-40. 10.1016/j.gloplacha.2014.06.005.
31. Raz-Yaseef N*, et al.* (2017) Evapotranspiration across plant types and geomorphological units in polygonal Arctic tundra. *Journal of Hydrology* 553:816-825. 10.1016/j.jhydrol.2017.08.036.
32. Boeskorov GG*, et al.* (2011) Woolly rhino discovery in the lower Kolyma River. *Quaternary Science Reviews* 30(17-18):2262-2272. 10.1016/j.quascirev.2011.02.010.
33. Kahlke R-D (1999) *The History of the Origin, Evolution and Dispersal of the Late Pleistocene Mammuthus-Coelodonta Faunal Complex in Eurasia (Large Mammals)* (Fenske Companies, Rapid City).
34. Deng T*, et al.* (2011) Out of Tibet: Pliocene Woolly Rhino Suggests High-Plateau Origin of Ice Age Megaherbivores. *Science* 333(6047):1285-1288. 10.1126/science.1206594.
35. Hutchinson GE (1957) Concluding remarks-cold spring harbor symposia on quantitative biology. *Bulletin of mathematical biology* 53(1507). 10.1007/978-3-642-68836-2_20.
36. Nogués-Bravo D (2009) Predicting the past distribution of species climatic niches. *Global Ecology and Biogeography* 18(5):521-531. 10.1111/j.1466-8238.2009.00476.x.
37. Pagani L*, et al.* (2016) Genomic analyses inform on migration events during the peopling of Eurasia. *Nature* 538(7624):238-242. 10.1038/nature19792.
38. Canteri E*, et al.* (2022) Spatiotemporal influences of climate and humans on muskox range dynamics over multiple millennia. *Global Change Biology*. 10.1111/gcb.16375.

39. Fordham DA*, et al.* (2022) Process-explicit models reveal pathway to extinction for woolly mammoth using pattern-oriented validation. *Ecol Lett* 25(1):125-137. 10.1111/ele.13911.
40. Pilowsky JA*, et al.* (2022) Range and extinction dynamics of the steppe bison in Siberia: a pattern-oriented modeling approach. *Global Ecology and Biogeography*. 10.1111/geb.13601.
41. Haythorne S, Fordham D, Brown SC, Buettel J, & Brook B (2021) poems: Pattern-Oriented Ensemble Modeling System.), 1.0.1. https://cran.r-project.org/package=poems
42. Goodrich B, Gabry J, Ali I, & Brilleman S (2020) rstanarm: Bayesian applied regression modeling via Stan), 2.21.1. https://mc-stan.org/rstanarm
43. Blonder B*, et al.* (2018) New approaches for delineating n-dimensional hypervolumes. *Methods in Ecology and Evolution* 9(2):305-319. 10.1111/2041-210x.12865.
44. Dolédec S, Chessel D, & Gimaret-Carpentier C (2000) Niche Separation in Community Analysis: A New Method. *Ecology* 81(10):2914-2927. 10.1890/0012-9658(2000)081[2914:Nsicaa]2.0.Co;2.
45. Dray S & Dufour AB (2007) The ade4 package: Implementing the duality diagram for ecologists. *Journal of Statistical Software* 22(4):1-20. 10.18637/jss.v022.i04.
46. Elith J & Leathwick JR (2009) Species Distribution Models: Ecological Explanation and Prediction Across Space and Time. *Annual Review of Ecology, Evolution, and Systematics* 40(1):677-697. 10.1146/annurev.ecolsys.110308.120159.
47. Phillips SJ, Anderson RP, & Schapire RE (2006) Maximum entropy modeling of species geographic distributions. *Ecological Modelling* 190(3-4):231-259. 10.1016/j.ecolmodel.2005.03.026.
48. Boyce MS, Vernier PR, Nielsen SE, & Schmiegelow FKA (2002) Evaluating resource selection functions. *Ecological Modelling* 157(2-3):281-300. 10.1016/S0304-3800(02)00200-4.
49. Hirzel AH, Le Lay G, Helfer V, Randin C, & Guisan A (2006) Evaluating the ability of habitat suitability models to predict species presences. *Ecological Modelling* 199(2):142-152. 10.1016/j.ecolmodel.2006.05.017.
50. Fordham DA*, et al.* (2020) Using paleo-archives to safeguard biodiversity under climate change. *Science* 369(6507):1072-+. 10.1126/science.abc5654.
51. Eriksson A*, et al.* (2012) Late Pleistocene climate change and the global expansion of anatomically modern humans. *Proceedings of the National Academy of Sciences of the United States of America* 109(40):16089-16094. 10.1073/pnas.1209494109.
52. Raghavan M*, et al.* (2015) Genomic evidence for the Pleistocene and recent population history of Native Americans. *Science* 349(6250):aab3884. 10.1126/science.aab3884.
53. Lieth H (1975) Modeling the primary productivity of the world. *Primary productivity of the biosphere*, eds Lieth H & Whittaker RJ (Springer-Verlag, New York, USA).
54. Pilowsky JA, Manica A, Brown SC, Rahbek C, & Fordham DA (2022) Simulations of human migration into North America are more sensitive to demography than choice of palaeoclimate model. *Ecological Modelling*. 10.1016/j.ecolmodel.2022.110115.
55. Csillery K, Blum MG, Gaggiotti OE, & Francois O (2010) Approximate Bayesian Computation (ABC) in practice. *Trends Ecol Evol* 25(7):410-418. 10.1016/j.tree.2010.04.001.
56. Grimm V*, et al.* (2005) Pattern-oriented modeling of agent-based complex systems: lessons from ecology. *Science* 310(5750):987-991. 10.1126/science.1116681.
57. Fordham DA, Haythorne S, Brown SC, Buettel JC, & Brook BW (2021) poems: R package for simulating species' range dynamics using pattern-oriented validation. *Methods in Ecology and Evolution* 12(12):2364-2371. 10.1111/2041-210x.13720.
58. Haythorne S, Pilowsky J, Brown SC, & Fordham DA (2021) paleopop: Pattern-Oriented Modeling Framework for Coupled Niche-Population Paleo-Climatic Models), 2.1.2. https://cran.r-project.org/package=paleopop
59. Orlando L*, et al.* (2003) Ancient DNA analysis reveals woolly rhino evolutionary relationships. *Mol Phylogenet Evol* 28(3):485-499. 10.1016/s1055-7903(03)00023-x.
60. IUCN: The IUCN Red List of Threatened Species. https://www.iucnredlist.org
61. Pacifici M*, et al.* (2013) Generation length for mammals. *Nature Conservation-Bulgaria* 5(5):87-94. 10.3897/natureconservation.5.5734.

62. VanDerWal J, Shoo LP, Johnson CN, & Williams SE (2009) Abundance and the environmental niche: environmental suitability estimated from niche models predicts the upper limit of local abundance. *Am Nat* 174(2):282-291. 10.1086/600087.
63. Nowak RM (1999) *Walker's Mammals of the World* (The Johns Hopkins Univ. Press, Baltimore) 6 Ed.
64. Santini L, Benítez-López A, Dormann CF, & Huijbregts MAJ (2022) Population density estimates for terrestrial mammal species. *Global Ecology and Biogeography* 31(5):978-994. 10.1111/geb.13476.
65. Pusparini W, Sievert PR, Fuller TK, Randhir TO, & Andayani N (2015) Rhinos in the Parks: An Island-Wide Survey of the Last Wild Population of the Sumatran Rhinoceros. *PLOS ONE* 10(9):e0136643. 10.1371/journal.pone.0136643.
66. Miller PS*, et al.* (2015) *Population Viability Analysis for the Sumatran Rhino in Indonesia* (IUCN/SSC Conservation Breeding Specialist Group, Apple Valley, MN).
67. Ferreira SM*, et al.* (2015) Disruption of Rhino Demography by Poachers May Lead to Population Declines in Kruger National Park, South Africa. *PLOS ONE* 10(6):e0127783. 10.1371/journal.pone.0127783.
68. Ricker WE (1954) Stock and Recruitment. *Journal of the Fisheries Research Board of Canada* 11(5):559-623. 10.1139/f54-039.
69. Støen O-G, Pitlagano ML, & Moe SR (2009) Same-site multiple releases of translocated white rhinoceroses Ceratotherium simum may increase the risk of unwanted dispersal. *Oryx* 43(4):580-585. 10.1017/S0030605309990202.
70. Coady JW (1974) Influence of snow on behaviour of moose. *Naturaliste Canadien* 101:417-436.
71. Palkopoulou E*, et al.* (2015) Complete genomes reveal signatures of demographic and genetic declines in the woolly mammoth. *Curr Biol* 25(10):1395-1400. 10.1016/j.cub.2015.04.007.
72. Fordham DA*, et al.* (2013) Adapted conservation measures are required to save the Iberian lynx in a changing climate. *Nature Climate Change* 3(10):899-903. 10.1038/nclimate1954.
73. Pearson RG*, et al.* (2014) Life history and spatial traits predict extinction risk due to climate change. *Nature Climate Change* 4(3):217-221. 10.1038/Nclimate2113.
74. Bocherens H (2011) Diet and Ecology of Neanderthals: Implications from C and N Isotopes. *Neanderthal Lifeways, Subsistence and Technology: One Hundred Fifty Years of Neanderthal Study*, eds Conard NJ & Richter J (Springer Netherlands, Dordrecht), pp 73-85.
75. Weyrich LS*, et al.* (2017) Neanderthal behaviour, diet, and disease inferred from ancient DNA in dental calculus. *Nature* 544(7650):357-361. 10.1038/nature21674.
76. Wißing C*, et al.* (2019) Stable isotopes reveal patterns of diet and mobility in the last Neandertals and first modern humans in Europe. *Scientific Reports* 9(1):4433. 10.1038/s41598-019-41033-3.
77. Bevan A*, et al.* (2017) Holocene fluctuations in human population demonstrate repeated links to food production and climate. *Proceedings of the National Academy of Sciences* 114(49):E10524-E10531. 10.1073/pnas.1709190114.
78. Alroy J (2001) A Multispecies Overkill Simulation of the End-Pleistocene Megafaunal Mass Extinction. *Science* 292(5523):1893. 10.1126/science.1059342.
79. Brook BW & Bowman DMJS (2004) The uncertain blitzkrieg of Pleistocene megafauna. *Journal of Biogeography* 31(4):517-523. 10.1046/j.1365-2699.2003.01028.x.
80. Brook BW & Johnson CN (2006) Selective hunting of juveniles as a cause of the imperceptible overkill of the Australian Pleistocene megafauna. *Alcheringa: An Australasian Journal of Palaeontology* 30(sup1):39-48. 10.1080/03115510609506854.
81. Fordham DA, Haythorne S, & Brook BW (2016) Sensitivity Analysis of Range Dynamics Models (SARDM): Quantifying the influence of parameter uncertainty on forecasts of extinction risk from global change. *Environmental Modelling & Software* 83:193-197. 10.1016/j.envsoft.2016.05.020.
82. Prowse TAA*, et al.* (2016) An efficient protocol for the global sensitivity analysis of stochastic ecological models. *Ecosphere* 7(3):e01238. 10.1002/ecs2.1238.

83. van der Vaart E, Beaumont MA, Johnston ASA, & Sibly RM (2015) Calibration and evaluation of individual-based models using Approximate Bayesian Computation. *Ecological Modelling* 312:182-190. 10.1016/j.ecolmodel.2015.05.020.
84. Saltré F*, et al.* (2015) Uncertainties in dating constrain model choice for inferring extinction time from fossil records. *Quaternary Science Reviews* 112:128-137. 10.1016/j.quascirev.2015.01.022.
85. Joyce P & Marjoram P (2008) Approximately sufficient statistics and bayesian computation. *Stat Appl Genet Mol Biol* 7(1):Article26. 10.2202/1544-6115.1389.
86. Csilléry K, François O, & Blum MGB (2012) abc: an R package for approximate Bayesian computation (ABC). *Methods in Ecology and Evolution* 3(3):475-479. 10.1111/j.2041-210x.2011.00179.x.
87. Carnell R (2021) lhs: Latin Hypercube Samples), 1.1.3. https://cran.r-project.org/package=lhs
88. Makowski D, Ben-Shachar MS, & Lüdecke D (2019) bayestestR: Describing Effects and their Uncertainty, Existence and Significance within the Bayesian Framework. *Journal of Open Source Software* 4(40):1541. 10.21105/joss.01541.
89. Wang Y*, et al.* (2021) Late Quaternary dynamics of Arctic biota from ancient environmental genomics. *Nature* 600(7887):86-92. 10.1038/s41586-021-04016-x.
90. Coutts SR & Yokomizo H (2014) Meta-models as a straightforward approach to the sensitivity analysis of complex models. *Population Ecology* 56(1):7-19. 10.1007/s10144-013-0422-1.
91. Makowski D, Ben-Shachar MS, Chen SHA, & Lüdecke D (2019) Indices of Effect Existence and Significance in the Bayesian Framework. *Frontiers in Psychology* 10. 10.3389/fpsyg.2019.02767.
92. Rasmussen SO*, et al.* (2014) A stratigraphic framework for abrupt climatic changes during the Last Glacial period based on three synchronized Greenland ice-core records: refining and extending the INTIMATE event stratigraphy. *Quaternary Science Reviews* 106:14-28. 10.1016/j.quascirev.2014.09.007.
93. Anderson SC, Ward EJ, English PA, & Barnett LAK (2022) sdmTMB: an R package for fast, flexible, and user-friendly generalized linear mixed effects models with spatial and spatiotemporal random fields. *bioRxiv*. 10.1101/2022.03.24.485545.
94. Bakka H, Vanhatalo J, Illian JB, Simpson D, & Rue H (2019) Non-stationary Gaussian models with physical barriers. *arxiv*. 10.48550/ARXIV.1608.03787.
95. Barnett LAK, Ward EJ, & Anderson SC (2020) Improving estimates of species distribution change by incorporating local trends. *Ecography* 44(3):427-439. 10.1111/ecog.05176.
96. Gelman A (2006) Prior distributions for variance parameters in hierarchical models (comment on article by Browne and Draper). *Bayesian Analysis* 1(3):515-534. 10.1214/06-ba117a.
97. Hilbe JM (2012) *Negative Binomial Regression* (Cambridge University Press, Cambridge) 2 Ed.
98. Anselin L (1995) Local Indicators of Spatial Association—LISA. *Geographical Analysis* 27(2):93-115. 10.1111/j.1538-4632.1995.tb00338.x.